SENSORS & TRANSDUCERS

ISSN 1726-5479

vol. 266

3/24

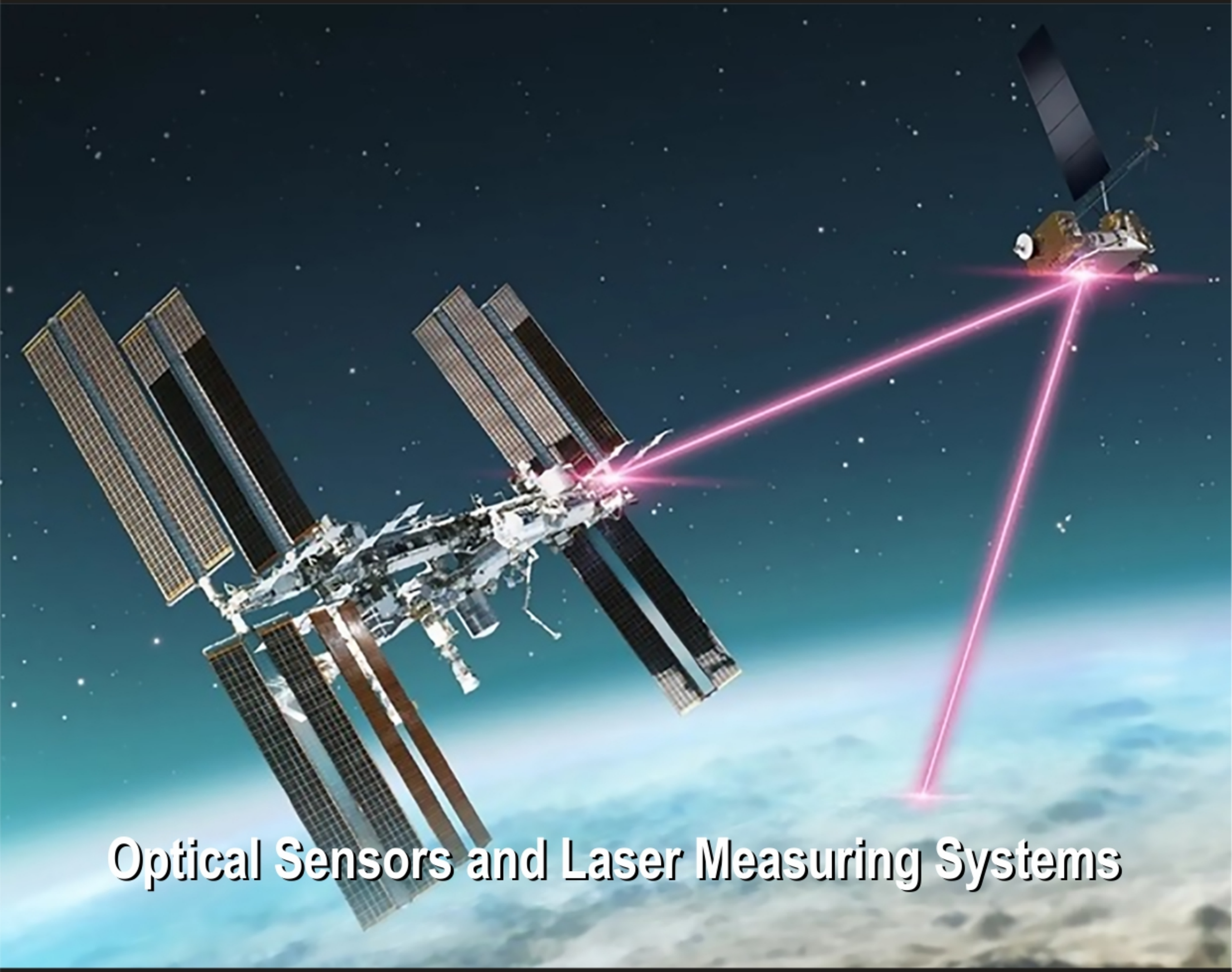

Optical Sensors and Laser Measuring Systems

International Frequency Sensor Association Publishing

IFSA

Sensors & Transducers

International Official Open Access Journal of the International Frequency Sensor Association (IFSA) Devoted to Research and Development of Sensors and Transducers

Volume 266, Issue 3, August 2024

IFSA Publishing: Barcelona • Toronto

Published by International Frequency Sensor Association (IFSA) Publishing. Printed in the USA.

Sensors & Transducers

Volume 266, Issue 3
August 2024

www.sensorsportal.com

e-ISSN 1726-5479
ISSN 2306-8515

Sensors & Transducers journal is an open access, peer review international journal published monthly by International Frequency Sensor Association (IFSA).
Available in both: print and electronic (printable pdf) formats.

Sensors & Transducers Journal

Contents

Volume 266
Issue 3
August 2024

www.sensorsportal.com

ISSN 2306-8515
e-ISSN 1726-5479

Research Articles

Authors are encouraged to submit article in MS Word (doc) and Acrobat (pdf) formats
by e-mail: editor@sensorsportal.com. Please visit journal's webpage with preparation instructions:
https://sensorsportal.com/st_guide_for_authors.html

International Frequency Sensor Association (IFSA).

10th International Conference on Sensors and Electronic Instrumentation Advances

https://www.seia-conference.com/

25-27 September 2024
Ibiza (Balearic Islands), Spain

The 10th annual SEIA' 2024 Conference is a key platform for sharing the latest in sensor and electronic instrumentation advancements, including AI-based sensor systems. It attracts global experts from academia and industry to discuss innovations in sensors, electronics, and measurement technologies. Since 2015, the event has been held in various locations, with the 2024 edition scheduled for 25-27 September in Ibiza, Spain, alongside the 6th IFSA Frequency and Time Conference and the 6th MicDAT Conference under the same conference umbrella. Organized by the International Frequency Sensor Association (IFSA) - one of the main professional association serving the sensor industry and academy since 1999, the SEIA' 2024 also emphasizes networking, featuring social events like a welcome cocktail, Gala Dinner, and farewell cocktail.

Sensor Technology

- Accelerometers
- Inclinometers
- Gyroscopes
- Mechanical Sensors
- Optical Sensors
- Optical Fiber Sensors
- Photonic Sensors
- Chemical Sensors
- Biosensors
- Immunosensors
- BioMEMS
- Temperature Sensors
- Pressure Sensors
- Acoustic Sensors
- Electromagnetic Sensors
- Gas Sensors
- Humidity Sensors
- Infrared Sensors, Devices and Thermography
- Radiation Sensors
- Multi Sensor Fusion
- Smart Sensors
- Intelligent Sensors
- Artificial Intelligence based Sensors and Sensor Systems
- Virtual Sensors
- Sensor Interfacing and Signal Conditioning
- Sensor Calibration
- Nanomaterials and Electronics Technology for Sensors
- Semiconductor Materials for Sensors
- Polymer Materials for Sensors
- MEMS and NEMS
- Remote Sensors and Telemetry
- Sensor Applications

Sensor Instrumentation and Measuring Technology

- Metrology and Measurement Science
- Methods of Measurements
- Calibrations and Standards
- Measurement of Electrical Quantities
- Time and Frequency Measurements
- Measurement of Force, Mass, Torque, Inclination and Acceleration
- Magnetic Measurements
- Hardness Measurements
- Measurement of Geometrical Quantities
- Temperature and Thermal Measurements
- Pressure and Vacuum Measurements
- Vibration and Noise Measurement
- Flow Measurements
- Chemical Measurements
- Quantum Measurements and Photonics
- Acoustics and the Ultrasonic Measurements
- Environmental Measurements
- Power and Energy Measurements
- Measurement of Human Functions
- Measurements in Biology and Medicine
- Mathematical Tools for Measurements
- Optical and Radiation Measurements
- Microwave Measurements
- Virtual Instruments and Data Acquisition Systems
- Soft Measurements
- Measurement Systems
- Distributed Measurements
- Analog-to-Digital Converters, Digital and Mixed Signal Processing
- Waveform Analysis and Measurements
- Scientific and Industrial Instrumentation
- Cyber-Physical Systems and IoT
- Experimental Mechanics
- Measurement in Robotics
- Metrology in Food and Nutrition
- Intelligent and Computer Vision Instruments
- Reliability of Instrument and Measurement Systems
- Nanometrology
- Technical Diagnostics and Testing
- Nondestructive Testing
- Blockchain Applications in Metrology and Measurements
- Education and Training in Measurement and Instrumentation

Special Sessions:

Authors are welcome to propose and manage special sessions during the SEIA' 2023. Each special session will contain 4-6 papers in a related field as specified above.

Session organizers will get: Certificate of Appreciation; Free Registration; Special Publishing Theme within Conference Proceedings.

Contribution Types:

- Keynote Presentations
- Invited Talks
- Special Sessions
- Regular Sessions
- Poster Sessions
- Special Sessions
- Online Sessions
- Exhibition

Deadlines:

Submission (2-page extended abstract):	**Open till now**
Notification of acceptance:	**In 2 weeks**
Registration:	**ASAP**
Camera ready and late registration:	**31 August 2024**

10th International Conference on Sensors and Electronic Instrumentation Advances

10th SEIA'24 IBIZA

https://www.seia-conference.com/

One event - three different publications !

1) All registered abstracts will be published in the conference proceedings (with the ISBN and DOI). Some previous SEIA Conference Series Proceedings are indexed in Conference Proceedings Citation Index (CPCI), Web of Science by Clarivate Analytics

2) Authors will be invited to submit full-page extended papers to special issue of one of affiliated open access journal.

3) The limited number of full-page papers published in the journals will be selected by the Editorial Board to extend to open access book chapters for the Book Series on 'Advances in Sensors: Reviews', Vol. 9, 'Advances in Biosensors: Reviews', Vol. 4 or 'Advances in Measurements and Instrumentation: Reviews', Vol. 3. These Book Series are indexed in the Book Citation Index (Wed of Science) by Clarivate Analytics.

Conference Hotel

The Ibiza Twiins Hotel
Av. Pere Matutes Noguera, 79, 07800 Ibiza, Spain

Social Programme

- Welcome Cocktail: 24 September 2024 (20:00-21:30).
- Gala Dinner: 26 September 2024 (20:00-23:30)
- Farewell Cocktail: 27 September 2024 (during the poster session)

Organizing Committee

Chairman
Prof., Dr. Sergey Y. Yurish (IFSA, Spain),
e-mail: seia@sensorsportal.com

Advisory Chairmen
Prof. Vijyakumar Varadarajan (The University of New South Wales, Australia)

Conference and Publication Manager
Tetyana Zakharchenko (IFSA Publishing, S.L., Spain)

Steering Committee:

Prof. Gennaro Conte (University Roma Tre, Italy)
Dr. Pavel Shuk (Saint-Gobain NorPro, USA)
Dr. Marius Gheorghe (Ideal Aerosmith, Inc., USA)
Dr. Paolo Dabove (Politecnico di Torino, Italy)
Prof. George Kiriakidis (European Materials Research Society (E-MRS), France)
Prof., Dr. Arkady Zhukov (Univ. of the Basque Country, Spain)

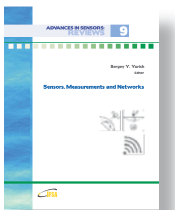

IFSA Publishing

F6S network partner

Sensors & Transducers, Vol. 266, Issue 3, August 2024, pp. 1-8

Sensors & Transducers
Published by IFSA Publishing, S. L., 2024
http://www.sensorsportal.com

Development of a Small-scale Spectrometer for Visible Light

[1, *] **Matthias HAUPT,** [1] **Sebastian SMARZYK,** [1] **Katharina STRATHMANN**
[1] Jade University of applied sciences, Friedrich-Paffrath-Straße 101,
26389 Wilhelmshaven, Germany
[1] Tel.: +49 4421 – 985 2625
[*] E-mail: matthias.haupt@jade-hs.de

Received: 23 April 2024 / Revised: 29 June 2024 / Accepted: 22 July 2024 / Published: 12 August 2024

Abstract: This paper details the development of a polymer-based miniaturized spectrometer as part of the "Minispectral" project at Jade University of Applied Sciences. The spectrometer's design leverages advanced injection molding techniques to create a polymer dome, which forms the core structure of the device. A concave diffraction grating is incorporated on the dome's surface to disperse incoming light into its constituent wavelengths. The dome and grating are designed with a generalized Rowland circle radius ratio in three-dimensional space, producing a lens effect for focused detection and analysis. Zemax ray tracing simulations are used to model the optical setup, while wave optics simulations, utilizing Rigorous Coupled-Wave Analysis (RCWA) implemented through Dynamic Link Libraries (DLLs) in Zemax, simulate critical parameters such as dome alignment, blazing, and the line density of the concave diffractive optical element (DOE). These simulations are vital for optimizing the spectrometer's performance. This paper presents the basic design, simulations, and the first test grating masters.

Keywords: Spectrometer, Polymer-based, Miniaturized, Injection molding, Diffraction grating, Optical simulations.

1. Introduction

Analyzing the optical spectrum of matter provides valuable insights into its chemical and molecular composition. In various applications, such as examining food, blood, or medications, miniaturized mobile spectrometers can serve as a time-saving alternative or valuable supplement to traditional stationary spectrometers typically used in laboratory settings. The primary objective of this project is to develop a polymer-based optic through a single manufacturing step. This is achieved by leveraging advanced injection molding technology and specially developed innovative tools. This paper not only focuses on the fundamental functions of the miniaturized spectrometer but also delves into its current development status. Chapter two and three present the concept of the spectrometer as showcased at the OPAL Conference '24 through a presentation and proceedings [1].

Starting from Chapter 3.1, the focus shifts to new findings, with particular emphasis on the initial fabrication of optical gratings.

2. Design of the Spectrometer

2.1. Basic Concept

The spectrometer utilized in this study is built upon the fundamental concept of a Rowland circle [2]. The three-dimensional dome shape of the optics enables efficient light guiding, thereby improving the signal-to-noise ratio (S/N) [3]. The specific geometry of the dome, coupled with a concave diffraction grating, allows all functions of a spectrometer to be fulfilled, eliminating the need for previously required individual components such as elaborate lens systems.

The operation of the spectrometer is illustrated in Fig. 1. Light enters through an input fiber into the polymer-based dome with a radius of r. At the end of the dome lies a mirrored, concave dispersion grating with a radius of 2r. This grating disperses the light into its individual wavelengths and reflects it back into the polymer dome. Due to the Rowland circle radius ratio of 2 to 1, the rays focus on the surface of the dome. A detector array is placed on the surface of the dome to detect the light decomposed into individual wavelengths and to utilize it for further analysis [4].

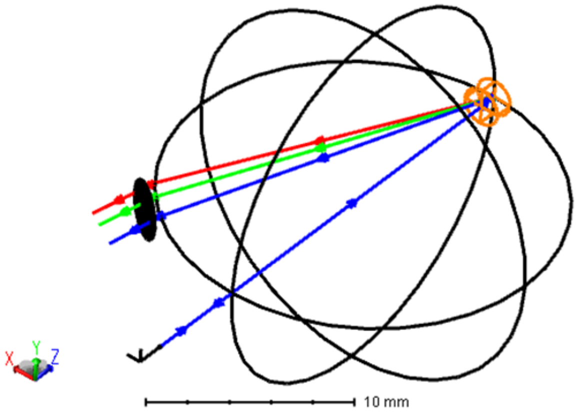

Fig. 1. Simulation created with Ansys Zemax to illustrate the concept of the spectrometer: The optics of the spectrometer are based on a polymer-based dome with a radius of r. A mirrored grating is applied to this dome, which has a curvature radius of 2r.

To better understand the system, Fig. 2 depicts a detailed drawing of the planned layout of the entire optics of the spectrometer. The dimensions are provided in millimeters, with the grating sphere having a radius of 20 mm and the input sphere having a radius of 10 mm. The drawing clearly illustrates the various components of the optical system. The grating sphere is shown as a circular structure, but it is important to note that only a small portion of it will be covered with the actual grating, where the light will interact. This grating will be precisely applied to this specific area to disperse the incoming light into its spectral components effectively. Similarly, the input sphere is prominently displayed, with a radius of 10 mm. This sphere serves as the entry point for light into the system. It is important to mention that the light into the input sphere will be coupled using an optical polymer fiber (POF), enhancing the precision of light transmission and alignment for accurate analysis. Additionally, the drawing features a rectangular thickening in the center, serving as a mounting bracket for the integration of the optical system into a larger framework. This strategic design facilitates the handling and installation of the spectrometer across various application scenarios.

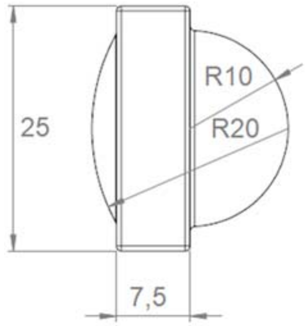

Fig. 2. Drawing depicting a planned layout of the entire optics of the spectrometer, showcasing dimensions in millimeters. It highlights the different radii, with the grating sphere at a radius of 20 mm and the input sphere at a radius of 10 mm. The rectangular thickening in the center may serve as a future mounting bracket for integration into a system.

2.2. Challenges of Curved Gratings Compared to Flat Gratings in Polymer-based DOEs

Curved gratings in polymer-based diffractive optical elements (DOEs) present unique challenges compared to their flat counterparts but also offer distinct advantages, including the exploitation of focal effects. Unlike flat gratings, curved gratings can be designed to focus light at specific points or along specific paths, enabling enhanced light manipulation and control. This focal effect can be harnessed for various applications, including beam shaping, spectral focusing, and aberration correction. In spectroscopy, curved gratings hold immense potential for improving the resolution and sensitivity of optical systems. Precisely controlling the curvature and geometry of the grating allows for tailoring the dispersion characteristics to achieve optimal spectral resolution and efficiency.

The production of curved gratings in polymer-based diffractive optical elements (DOEs) presents a unique set of challenges compared to their flat counterparts, primarily concerning fabrication methods and associated difficulties. Unlike flat gratings, which can be relatively straightforward to manufacture using techniques such as photolithography or electron beam lithography on planar substrates, the fabrication of curved structures requires more intricate processes. One significant hurdle lies in achieving precise and uniform curvature profiles across the polymer substrate. Traditional lithographic techniques may struggle to pattern curved surfaces accurately, leading to deviations from the desired geometry and potentially compromising optical performance.

Traditional lithographic techniques struggle with accurate pattern replication on curved substrates, prompting the development of advanced manufacturing methods such as nanoimprint lithography, hot embossing, and ultraprecision machining (UPM). Nanoimprint lithography and hot embossing enable the replication of complex curvature profiles with high precision, while UPM offers direct machining of curved surfaces with submicron accuracy. These methods address the need for precise curvature profiles and feature replication, though challenges such as material compatibility and scalability persist.

2.3. Optical Simulation

Raytracing simulations through Zemax software are utilized to ascertain the optimal dimensions of both the diffraction grating radius and dome radius, particularly when dealing with a large numerical aperture (NA), as observed in optical polymer fibers (POF). The polymer dome's diameter is targeted to be no more than 10 mm. Unfortunately, ray tracing is insufficient for accurately modeling diffractive optical elements due to its inherent limitation in accurately representing diffraction phenomena. Diffractive optical elements manipulate light through interference patterns rather than simple ray propagation, so more sophisticated computational methods are needed.

Various mathematical models can be considered for simulating curved optical gratings, including Finite Difference Time Domain (FDTD) and Finite Element Method (FEM). However, among these options, Rigorous Coupled-Wave Analysis (RCWA) emerges as a promising choice. RCWA offers precise solutions to Maxwell's equations while maintaining computational efficiency and adaptability to different geometries and materials. Compared to methods such as FDTD and FEM, RCWA excels in accuracy, computational speed, and ease of parameter exploration. These features make RCWA an attractive option to effectively model curved grating systems.

Within Zemax, the diffraction grating is simulated using Dynamic Link Libraries (DLLs) and employing RCWA. This allows dynamic adjustment and simulation of key parameters such as the curvature radius and blazing of the grating. The grating is anticipated to have a line density of up to 1000 lines/mm, with the objective of achieving a resolution of less than 1 nm.

The optical path depicted in Fig. 1 was simulated using the simulation software Ansys Zemax OpticStudio for various combinations of wavelengths and radii. As illustrated in Fig. 1, three wavelengths (400 nm, 550 nm, 650 nm) and a Rowland circle radius of 10 mm were considered. The grating has a line density of 1000 lines/mm. Aluminum emerges as a promising material for mirroring the grid, as it enhances reflectivity in the visible spectrum [5]. Therefore, it was assumed for this purpose in the simulation. In this case, the entrance aperture of the spectrometer has a diameter of 1 mm, corresponding to the diameter of a standard SI polymer optical fiber (POF) [6]. To optimize the performance further, extensive parametric studies were conducted within Zemax, exploring a wider range of parameters such as different grating materials, variations in dome diameter, and line densities. These simulations were crucial in refining the design parameters to achieve superior optical performance, especially in terms of resolution and spectral efficiency. Furthermore, the simulations allowed for the identification of potential challenges and trade-offs, enabling informed decision-making during the design process. Overall, the comprehensive simulation approach facilitated the development of a robust and efficient spectrometer system tailored to the specific requirements of optical polymer fibers.

2.4. Challenges in Optical Injection Molding with Aluminum Coating

Injection molding optical components poses inherent challenges such as achieving smooth surfaces, managing thermal stresses, and ensuring precise mold design. Despite these hurdles, we've opted to utilize PMMA for our initial demonstrator due to its favorable optical properties. Optical injection molding with subsequent aluminum coating application presents several challenges, encompassing both technological intricacies and process-related considerations. Initially, the injection molding process must ensure precise replication of complex geometries or thin-walled structures on the substrate material. Once the molding is complete, the application of the aluminum coating poses additional challenges. Achieving uniform distribution and proper adhesion of the aluminum onto the molded part becomes crucial, considering the specialized properties of aluminum coatings. Thermal stresses generated during the coating process could potentially compromise the optical characteristics or integrity of the coating, necessitating careful temperature control. When exploring methods for applying the aluminum coating, sputtering emerges as a promising option due to its ability to achieve uniform thickness and excellent adhesion onto substrates. While other techniques such as physical vapor deposition (PVD), chemical vapor deposition (CVD), and thermal spraying offer alternatives, sputtering appears particularly well-suited for this application. However, the selection of the most suitable method depends on factors such as substrate material, coating thickness requirements, and production volume. Thorough consideration of these factors is essential to determine the optimal coating method, ensuring the production of high-quality optical injection molded parts with aluminum coating.

3. Manufacturing and Characterization

Following the simulations and laboratory pre-tests, the production of initial demonstrators ensues. Here, the dome will be manufactured using state-of-the-art injection molding technology in a single process step. The fabrication of the grating on the surface of the polymer dome is proposed to be executed through Ultra-Precision Machining (UPM). This involves a manufacturing technique where very small layers of the material's surface are removed using diamond tools. UPM enables the creation of highly precise structures with sub-micrometer tolerance deviations, making it suitable for producing spherical and aspherical surfaces with high optical quality [7]. The initial demonstrators thus produced will undergo thorough examination and characterization in the laboratory. To ensure the accuracy of the grating structures, an Atomic Force Microscope (AFM) will be employed. AFM provides high-resolution imaging and precise measurements at the nanometer scale, allowing for detailed analysis of surface features. This step is crucial as it ensures that the manufactured gratings match the intended specifications with minimal deviation. Subsequently, the findings will be compared with the simulation results. Leveraging these insights, the optics parameters and production workflows will be optimized to enhance the subsequent generation of spectrometers. This achievement sets the stage for the near-future launch of the first fully functional, miniaturized spectrometer, utilizing polymer-based materials. Expanding upon this process, once the initial demonstrators are successfully produced, a comprehensive evaluation will be conducted to validate their performance under various conditions and operational scenarios. This evaluation will involve a meticulous analysis of the spectral data obtained from the spectrometer, assessing its accuracy, resolution, and sensitivity. Building upon the insights gained from both experimental evaluations and computational simulations, iterative refinements will be made to the optics parameters and production workflows. This iterative process will aim to enhance the overall performance, reliability, and manufacturability of the miniaturized spectrometer.

Additionally, advancements in material science and manufacturing technologies will be explored to further push the boundaries of performance and miniaturization.

3.1. Fabrication of Initial Gratings in Nickel Phosphorus

Nickel phosphorus offers several advantages for the fabrication of optical gratings, particularly with lattice constants around 1 µm, due to its unique properties, primarily its non-crystalline structure. Unlike crystalline materials, nickel phosphorus is amorphous, lacking defined crystal grains or axes. This characteristic reduces scattering and interference effects in optical applications, allowing for the production of high-resolution and precise optical gratings with minimal side effects. The amorphous nature of nickel phosphorus also ensures a uniform refractive index distribution across the grating surface, essential for accurate dispersion of light into different wavelengths and the mitigation of optical aberrations. Despite its non-crystalline structure, nickel phosphorus maintains high mechanical stability, crucial for long-term performance and reliability of grating structures in optical devices. Furthermore, nickel phosphorus exhibits excellent chemical resistance, enhancing the durability of gratings in diverse environmental conditions [8]. Its chemical composition and amorphous structure facilitate the precise fabrication of fine gratings with lattice constants as small as 1 micron, meeting the stringent requirements of high-resolution optical applications. In summary, the combination of amorphous properties, precise manufacturability, good optical characteristics, mechanical stability, and chemical resistance makes nickel phosphorus an ideal material for producing optical gratings with small lattice constants in the micron range.

3.2. Investigating Nickel Phosphorus Gratings

Gratings fabricated in nickel phosphorus using a monocrystalline diamond tip were thoroughly investigated in this study. Three distinct grating designs with lattice constants of 1 µm, 1.5 µm, and 2 µm, each featuring a 60° blazing angle, were subjected to detailed examination using both Atomic Force Microscopy (AFM) and scanning electron microscopy (SEM). AFM provided precise measurements of surface topography, including grating pitch and depth, offering insights into the structural dimensions critical for optical performance.

SEM analysis, on the other hand, delved into the internal structure and composition of the gratings, examining crystalline quality and potential defects. In addition to microscopy, diffraction efficiency measurements were conducted across various wavelengths to assess optical performance.

SEM analysis, on the other hand, delved into the internal structure and composition of the gratings, examining crystalline quality and potential defects. In addition to microscopy, diffraction efficiency measurements were conducted across various wavelengths to assess optical performance.

Figs. 3 to 8 depict scanning electron microscopy (SEM) and atomic force microscopy (AFM) images of the investigated grids. These images provide detailed insights into the structural characteristics and surface morphology of the grids under study. Through meticulous analysis, the lattice constants have been precisely determined to be 1 µm, 1.5 µm, and 2 µm, indicating the varied periodicity across different samples. Notably, the fabrication process has demonstrated the capability to produce homogeneous grids over extensive areas, suggesting robust manufacturing techniques. However, upon closer examination, a minor undulation is noticeable at the apex of the grooves, which could potentially influence the functional properties of the grids. The depth of the grid structures measures approximately 0.5 µm, underscoring their substantial structural integrity and depth profile. Nonetheless, further investigations are required to verify the blazing angle, a critical parameter influencing the optical performance of the grids. This ongoing verification process aims to ensure accurate and consistent measurement of this angle across all samples. In summary, the SEM and AFM images provide valuable data confirming the uniformity and structural characteristics of the grids, while also highlighting areas for potential refinement and optimization in future manufacturing processes. This version expands on the details of the SEM and AFM images, discusses the precision of lattice constants, mentions surface characteristics, and emphasizes the need for further verification of the blazing angle, providing a comprehensive overview of the findings.

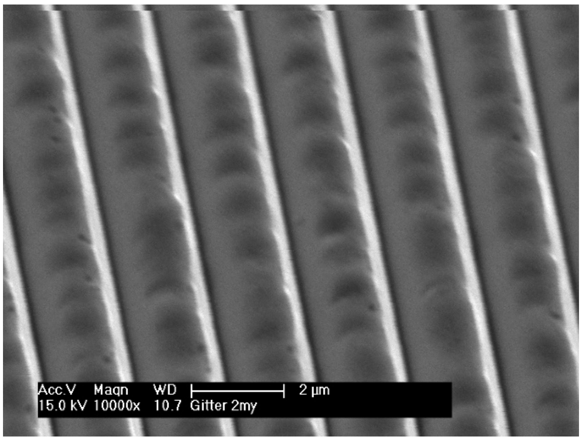

Fig. 3. SEM image of an investigated grid at 10,000× magnification. The image clearly shows the regular grid structures with a lattice constant of 2 µm. Minor irregularities are visible at the tips of the grooves.

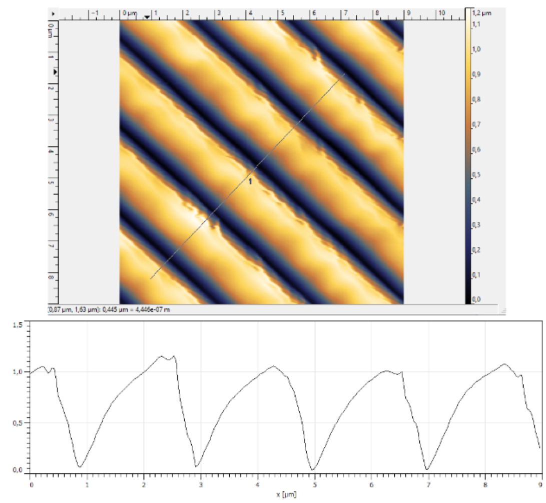

Fig. 4. AFM image of the same grid as shown in Fig. 3. The image displays the three-dimensional topography of the grid structures with a lattice constant of 2 µm. Surface fluctuations along the grid grooves are evident.

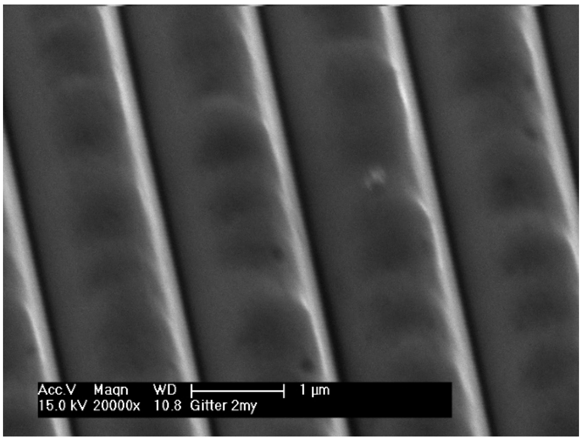

Fig. 5. SEM image of an investigated grid at 20,000× magnification. The image clearly shows the regular grid structures with a lattice constant of 1.5 µm. Minor irregularities are visible at the tips of the grooves.

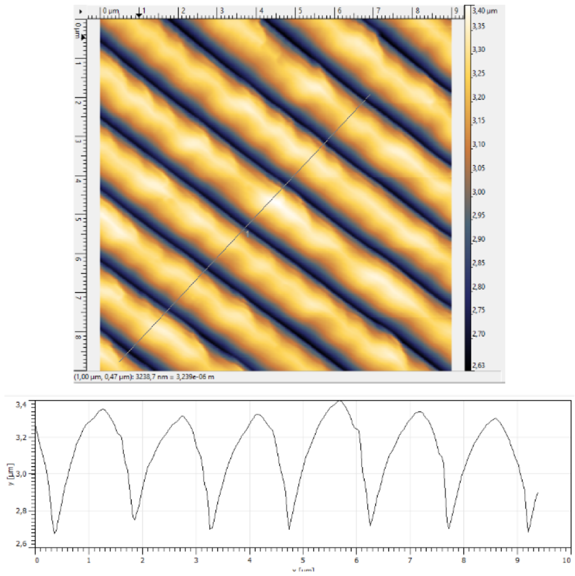

Fig. 6. AFM image of the same grid as shown in Fig. 5. The image displays the three-dimensional topography of the grid structures with a lattice constant of 1.5 µm. Surface fluctuations along the grid grooves are evident.

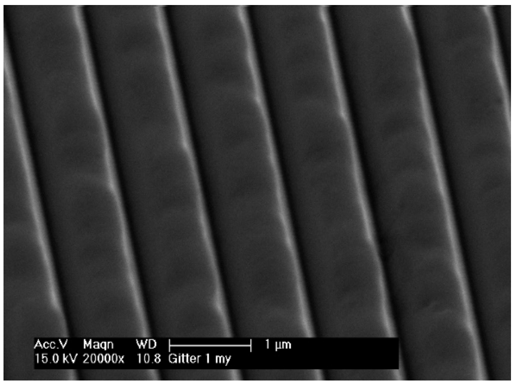

Fig. 7. SEM image of an investigated grid at 20,000× magnification. The image clearly shows the regular grid structures with a lattice constant of 1 µm. Minor irregularities are visible at the tips of the grooves.

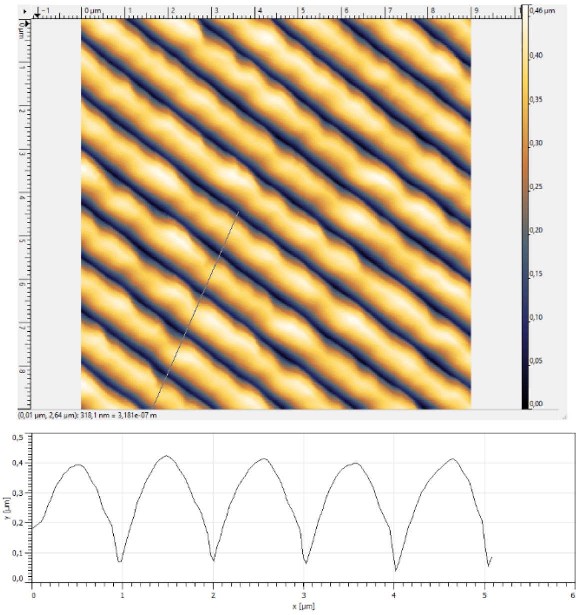

Fig. 8. AFM image of the same grid as shown in Fig. 7. The image displays the three-dimensional topography of the grid structures with a lattice constant of 1 µm. Surface fluctuations along the grid grooves are evident.

SEM image at 5000× magnification displaying a grid structure with a consistent lattice constant of 1 µm. The image vividly illustrates the uniformity of the grid pattern across a substantial area. This high degree of consistency underscores the precision and reliability of the manufacturing process in producing intricate microscale features. This observation is particularly evident in Fig. 9.

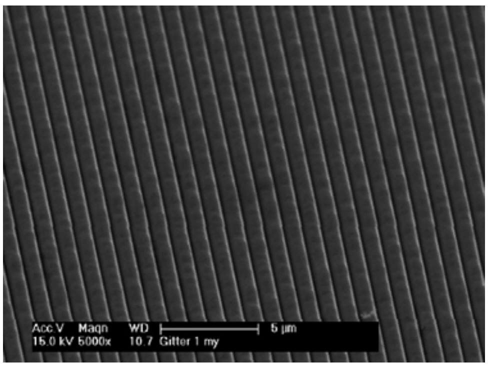

Fig. 9. SEM image at 5000× magnification showcasing a grid structure with a precise lattice constant of 1 µm. The image reveals the remarkable homogeneity of the grid pattern across an extensive area. This level of uniformity underscores the effectiveness of the fabrication process in achieving consistent microscale features.

3.2. From Nickel Phosphorus to Reflective Optics: Molding and Characterization Process

The next phase involves transferring the fabricated grids made from nickel phosphorus into silicone molds. This transfer process is crucial as it ensures the replication of intricate grid patterns with high fidelity. The grids are meticulously embedded into silicone, leveraging its moldability to capture the precise details of the nickel phosphorus structure. Once molded, these grids undergo thorough optical inspection to analyze their diffraction properties as transmissive gratings. This examination aims to verify the accuracy of the silicone replication process in preserving the intended diffraction orders and spatial characteristics of the original grids. Following the transmissive analysis, the grids undergo a crucial enhancement step by being coated with a layer of silver. This silver coating serves multiple purposes: it enhances the reflectivity of the grids and provides durability against environmental factors, ensuring long-term optical performance. After silver coating, the grids are subjected to further scrutiny using advanced microscopy techniques such as Scanning Electron Microscopy (SEM). This examination verifies the exactness of the silicone molding process and ensures that the silver coating adheres uniformly across the grid surfaces, maintaining the precision required for their optical functionality. Once the structural integrity and coating uniformity are confirmed, the grids are reassessed for their optical characteristics, this time as reflective gratings. The reflective properties are meticulously evaluated to assess factors such as reflectance efficiency, spectral response, and overall optical quality. This evaluation phase is critical as it validates the grids' performance as reflective optical elements suitable for various applications in optics and photonics. In summary, the transformation of nickel phosphorus grids into silicone molds, followed by optical inspection, silver coating, and final reflective evaluation, underscores a meticulous process aimed at ensuring the grids' functionality and reliability as high-performance optical components.

4. Outlook

This chapter introduces a forward-looking perspective split into two essential areas: simulation and manufacturing. We explore how virtual simulations and actual production processes interact and evolve, reshaping efficiency and precision.

4.1. Simulation

Continuing from our previous chapters where simulations were conducted and physical optical grids were fabricated and measured, this section marks a critical advancement: integrating these measured grids into a digital simulation environment. Our goal now is to accurately translate real-world measurements into a virtual context. This includes capturing detailed dimensions, angles, and spatial relationships with precision, ensuring that our digital simulation faithfully represents the physical grids created earlier.

Optical simulations are instrumental in this process, facilitated through advanced software such as Zemax. Utilizing sophisticated computational algorithms and modeling techniques inherent in Zemax, our aim is to faithfully replicate the optical properties of the measured grids. By inputting these measured data points into Zemax, we create virtual models that simulate how light interacts with these optical structures. This process not only validates our simulations but also enables us to predict and optimize optical performance across different scenarios.

In Fig. 10, we present a visualization of the grid simulation implemented in Zemax using an RCWA DLL (Rigorous Coupled Wave Analysis Dynamic Link Library). This implementation allows the grid to be replicated layer by layer within the software environment. Our objective is to systematically recreate the measured structures, refining the simulation iteratively to achieve accurate representation.

4.2. Manufacturing

In the manufacturing process, there are several critical considerations to keep in mind for the next step. One of the foremost tasks is the creation of a stamp. This stamp must be designed in such a way that its microstructures can be accurately replicated not only in silicone but also in other polymers, such as polymethyl methacrylate (PMMA). This requirement demands a precise understanding of the material properties and the behavior of these polymers during the replication process. The stamp’s microstructures must maintain their integrity and detail across different materials to ensure the fidelity of the replicated patterns. Additionally, there is the challenge of shaping a curved grating surface. Unlike planar surfaces, curved surfaces introduce complexities in both the design and manufacturing stages. These complexities arise from the need to ensure that the grating’s microstructures are uniformly transferred onto a non-flat surface. Achieving this requires advanced techniques and tools capable of handling the intricacies involved in curving the grating while preserving the desired optical properties. The gratings presented in section three are currently planar, which simplifies the manufacturing process to a certain extent. Planar gratings are easier to produce and replicate because they do not involve the added complexity of working with curved surfaces. However, the transition to curved gratings is a necessary step to meet the evolving requirements of various applications. Curved gratings can offer enhanced performance and new functionalities that planar gratings cannot provide. To successfully move from planar to curved grating surfaces, it is essential to develop a thorough understanding of how to control the replication process on a curved geometry. This includes investigating the optimal conditions for transferring microstructures onto curved surfaces and ensuring that the mechanical and optical properties of the gratings are not compromised. Furthermore, the manufacturing techniques must be adapted or even redesigned to accommodate the new geometrical challenges posed by curved surfaces. In summary, the next step in the manufacturing process involves careful consideration of two main aspects: the creation of versatile stamps capable of replicating microstructures in various polymers, and the development of methods to shape and replicate curved grating surfaces.

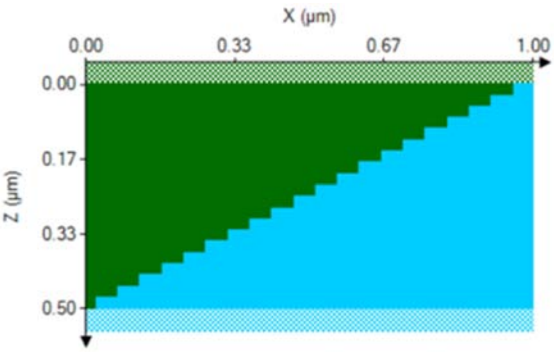

Fig. 10. Visual representation of the optical grid simulation in Zemax utilizing Rigorous Coupled Wave Analysis Dynamic Link Library (RCWA DLL). The grid structure is modeled layer by layer, exemplifying parameters such as a lattice constant of 1 µm, a blaze angle of 63°, and a grid depth of 0.5 µm. The simulation calculation includes 20 uniformly decreasing layers, aiming to systematically replicate and validate measured optical structures.

5. Conclusions

In summary, our research highlights the progress made in developing a miniaturized spectrometer based on polymer optics. By integrating modern injection molding technology with innovative design principles, we’ve achieved a compact yet efficient analytical tool suitable for diverse applications such as food analysis, medical diagnostics, and pharmaceutical quality control. In this context, we have also elucidated the fundamental concept of the spectrometer. Additionally, we have presented the first grids made from nickel-phosphorus and examined their structures using Scanning Electron Microscopy (SEM) and Atomic Force Microscopy (AFM). The successful simulation and manufacturing of initial prototypes signify a significant step forward in spectroscopic instrumentation. Further refinement through laboratory characterization and optimization of production workflows will enhance the performance and scalability of this technology, facilitating its integration into various industrial and scientific settings. This advancement holds the promise of revolutionizing spectral analysis, offering a practical and accessible solution for rapid chemical and molecular composition determination.

Acknowledgements

This Project is supported by the Federal Ministry for Economic Affairs and Climate Action (BMWK) on the basis of a decision by the German Bundestag.

References

[1]. M. Haupt, S. Smarzyk, K. Strathmann, Design and development of a miniature spectrometer for the visible wavelength region, in *Proceedings of the 7th International Conference on Optics, Photonics and Lasers (OPAL'24)*, 2024, pp. 58-61.

[2]. H. A. Rowland, XXIX. On concave gratings for optical purposes, *Philosophical Magazine Series 5*, Vol. 16, Issue 99, 1883, pp. 197-210.

[3]. S. Höll, M. Haupt, U. H. P. Fischer, Design and development of an injection-molded demultiplexer for optical communication systems in the visible range, *Appl. Opt*., Vol. 52, 2013, pp. 4103-4110.

[4]. S. Smarzyk, H. Lass, Entwicklung eines miniaturisierten Spektrometers für den optischen Wellenlängenbereich, DGAo Proceeding, 2023, https://www.dgao-proceedings.de/download/124/124_p5.pdf

[5]. G. Hass, J. E. Waylonis, Optical constants and reactance and transmittance of evaporated aluminum in the visible and ultraviolet, *Journal of the Optical Society of America*, Vol. 51, Issue 7, 1961, 719.

[6]. S. Smarzyk, H. Lass, Simulationsberechnungen eines Spektrometers mit Rowlandkreis und Simulation einer Eintrittsöffnung mit großer NA, Tagungsband NWK 2023, https://www.hs-harz.de/dokumente/extern/Forschung/NWK2023/TagungsbandNWK2023. Pdf

[7]. W. B. Lee, B. C. F. Cheung, Surface Generation in Ultraprecision Diamond Turning: Modelling and Practices, Engineering Research Series (REP), *Wiley*, 2003.

[8]. H. Nazari, G. Darband, R. Arefinia, A review on electroless Ni-P nanocomposite coatings: effect of hard, soft, and synergistic nanoparticles, *Journal of Materials Science*, Vol. 58, 2023, pp. 4292-4358.

Published by International Frequency Sensor Association (IFSA) Publishing, S. L., 2024 (http://www.sensorsportal.com).

Sensors & Transducers, Vol. 266, Issue 3, August 2024, pp. 9-15

Sensors & Transducers
Published by IFSA Publishing, S. L., 2024
http://www.sensorsportal.com

Contrasting Laser Ablation and Photon Pressure Propulsion

[1, *] Claude PHIPPS, [2] Gediminas RACIUKAITIS, [3] Séverine A. E. BOYER
[1] Photonic Associates, LLC, 200A Ojo de la Vaca Rd, Santa Fe, NM, 87508, USA
[2] FTMC – Center for Physical Sciences and Technology, Savanoriu Ave. 231, Vilnius 02300, Lithuania
[3] CNRS7635-CEMEF, MINES ParisTech PSL, Sophia Antipolis, France
[1] Tel.: +1-215-358-4360, fax: +1-505-466-3877
[*] E-mail: crphipps@aol.com

Received: 23 April 2024 / Revised: 21 July 2024 / Accepted: 9 August 2024 / Published: 12 August 2024

Abstract: In this article, we contrast laser ablation propulsion with photon pressure propulsion. LAP must use repetitive short pulses (~100 ps) for best performance, while PPP requires GW-level continuous (CW) lasers and a lightsail to receive the beam and drag the payload to relativistic speeds.

Keywords: Photon pressure propulsion, Breakthrough starshot, Laser ablation propulsion, Relativistic travel, Alpha Centauri.

1. Introduction – Comparing LAP and PPP

This idea was briefly treated in [1].

The beam parameters [2] which are important for laser propulsion are similar for laser ablation propulsion (LAP) and pure photon propulsion (PPP). These are:

Momentum coupling coefficient Cm,

$$C_m = F / P_{inc}, \tag{1}$$

the ratio of thrust F to incident laser power $Pinc$. with dimensions N/W,

For LAP, a specific impulse is given by

$$I_{sp} = v_E / g_o \tag{2}$$

exhaust velocity v_E divided by the acceleration of gravity (a rocketry term with dimensions of seconds), and Thermal coupling coefficient

$$C_{th} = Q / W \tag{3}$$

For LAP, Cth is important because deposited heat Q can melt the target before the mission is finished. For PPP it is also important to avoid melting the lightsail.

For LAP, ablation kinetic efficiency is

$$\eta_{AB} = \delta m v_E^2 / (2W) = C_m I_{sp} g_o / 2, \tag{4}$$

a dimensionless quantity where δm is the single pulse ablated mass. For PPP,

$$\eta = \gamma m_o c^2 / (Pt), \tag{5}$$

allowing for relativistic speeds, where

$$\gamma = \frac{1}{\sqrt{1-\beta^2}}, \tag{6}$$

β = v/c, m_o is the rest mass, *c* is light speed, *P* is laser power, and *t* is the CW beam duration.

Figs. 1 and 2 compare the mechanics of this interaction in the two cases. $\bar{E}$ indicates the direction of the associated optical electric field, giving initial surface breakdown and plasma formation in the case of LAP, which are critical for efficient propulsion. The factor of 2 for impulse in Fig. 2 assumes perfect reflection.

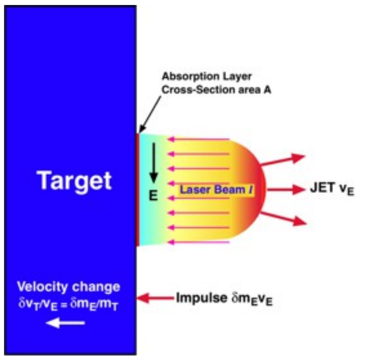

Fig. 1. Illustrating momentum generation for LAP.

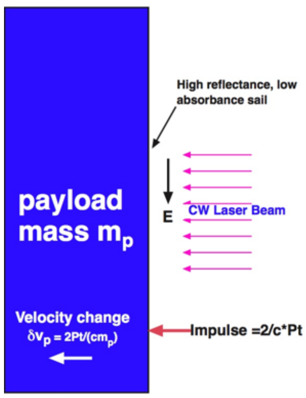

Fig. 2. Illustrating impulse for PPP for zero velocity and zero absorption.

Related quantities involving these basic parameters are:

Ablated mass depth for a single shot in LAP is

$$\delta x = C_m^2 \Phi / (2\rho_T \eta_{AB}), \quad (7)$$

where ρ_T is the target mass density, and Φ is the incident pulse fluence (J/m^2), and δx = 0 for PPP,

Ablation fuel lifetime for LAP is

$$\tau_{AB} = 2M\eta_{AB} / (PC_m^2), \quad (8)$$

for LAP, where *M* is the ablation fuel mass. Thrust

$$F = C_m P, \quad (9)$$

for LAP. To allow for relativistic speeds, a more complicated relationship exists for PPP,

$$F = \gamma^3 m_o c\dot{\beta}, \quad (10)$$

If τ_{AB} is less than mission lifetime *T*, a laser-propelled craft will not reach its destination.

For PPP, $\tau = \infty$, providing care is taken with sail temperature. Therefore, relativistic speeds are possible in PPP, which is a strong advantage over LAP for some missions.

Optimum values for all these parameters can be chosen for any problem.

For LAP, there are several optima, each giving different sets of laser parameters: delivered mass ratio m/M, cost per kg and delivered mass m.

C_{th} is critically important for LAP because the target will melt after N_{max} pulses when it is a simple object with mass *M* that shares all the incident energy [1]

$$N_{max} = (2/3)^{1/3} C_p M (T_m - T_i) / (C_{th} W), \quad (11)$$

If the target is space debris, melting will create much more debris. For Al in LAP, N_{max} predicted by (11) is of order 2000 pulses, whereas millions of pulses may be required to complete some propulsion tasks. In Eq. (11), T_m is the melting temperature, and C_p is the target material's specific heat.

We have shown that reality is more complex than this in LAP, and the material can take many more pulses than in Eq. (11). At very high laser intensity, surface recession can outrun the thermal wave [2], giving

$$v_{rec} / v_{th} \propto \frac{\sqrt{\Phi} A^{1/8}}{\sqrt{\lambda \rho K} \tau^{1/4} [Z^2(Z+1)]^{3/8}} >> 1, \quad (12)$$

and appropriately larger N_{max}. In Eq. (12), *Z* is the plasma atom charge state, *A* is atomic mass, λ is wavelength and τ is pulse duration.

For cases where we can choose a target material, we obviously want to select a material with very low thermal conductivity K and C_{th} value but very large ablation efficiency η_{AB} and large melting temperature T_m. If we select target materials like ZrO_2 or $CaCO_3$, we have shown that N_{max} can be thousands of times larger than for bulk Al [4], but only for short pulses.

In PPP, the laser is continuous (CW), and the maximum duration is governed only by lightsail temperature, limited by reradiation.

Relativistic propulsion using just pure light pressure without ablation is key to the Breakthrough Starshot proposal. This is the only way in which humans (or instruments) will explore regions within a few light years of Earth.

For PPP, given

$$D=\sqrt{\frac{1+\beta}{1-\beta}},\quad (13)$$

for the relativistic Doppler factor of the lightsail relative to the laser, the equation of motion is

$$\frac{d\beta}{dt}=c\beta\frac{d\beta}{dz}=\frac{(A+2R)P}{c^2 m_o D^2\gamma^3},\quad (14)$$

where P is the laser power received by the lightsail in the laser frame with absorbance A and reflectivity R. In Eq. (14), γ is the time dilation factor in Eq. (6).

For PPP, kinetic energy is given by

$$KE=\gamma m_o c^2\quad (15)$$

For the PPP case, in which travel beyond the solar system is the goal, we will discuss the likelihood of finding intelligent extraterrestrial life in subsequent sections.

Using parameters anticipated for Breakthrough Starshot, Table 1 shows the results for $\beta=0.2$, Table 2 gives results for $\beta=0.7$ and Table 3 outlines the results for $\beta=0.99$. Table 4 is a summary.

Table 1. β = 0.2 [5].

Sail diameter (m)	4.0
Payload mass (kg)	0.0035
Energy efficiency η (%)	3.0
Laser aperture diameter (m)	180
Beam transmit duration (s)	500
Temperature limited force (N)	500
Irradiance (GW/m^2)	8.7
Peak laser power (GW)	260
Temperature limited acceleration (G)	15k
Goal (light years)	4.37
Time to goal (Earth years)	22
Cost (B$)	8.98

Table 2. β = 0.7 [5].

Sail diameter (m)	4k
Payload mass (kg)	20k
Energy efficiency η (%)	26
Laser aperture diameter (m)	1.8k
Beam transmit duration (mo)	2.7
Temperature limited force (N)	260k
Irradiance (GW/m^2)	17.5
Peak laser power (PW)	220
Temperature limited acceleration (G)	3.4
Goal (light years)	12
Time to goal (onboard years)	12
Cost (T$)	10.5

2. Details of Breakthrough Starshot Flight

This flight will be quite expensive per kg payload mass because it is the first, and a lot of infrastructure has to be built. In 500 s, the lightsail and payload will reach 0.2c and be located at about 1/3 the distance from Earth to Mars at the closest approach, way beyond the Moon. At the end of one day, the payload will be twice the distance from Earth to Pluto on its closest approach to us. Still, it will take 22 years to reach Alpha Centauri. The lightsail has to withstand 870 kW/cm^2 irradiance. In order not to burn up, the point design calls for its absorptance to be less than 10^{-8} [5]. The Starshot designers believe they can achieve this.

One thing was not made clear: to transmit photos of the Alpha Centauri region back to Earth, the payload also needs to include a 4-m diameter transmitting aperture. However, Dr Parkin tells me that will be the parabolic shape of the lightsail itself, so it will not increase payload mass and the required laser power or lightsail area.

Table 3. β = 0.99 [5].

	Distance (ly)	**Duration seen from Earth (y)**	**Duration on board lightsail with braking (y)**	**Duration on board lightsail, no braking (y)**
Acceleration	15.34	16.0	3.68	3.68
Cruise	69.32	70.0	9.78	9.88
Deceleration	15.34	16.0	3.68	2.26
Totals	100	102.0	17.14	15.81
Cost/kg	6.26B$			

Table 4. Summary [5].

	Distance (ly)	**Payload Mass**	**Duration (yr)**	**Max β**	**Sail dia. (m)**	**Max G's**	**Cost (Capex + Opex)**
Starshot	4.4	0.0035 kg	22	0.2	4	15 k	8.8 B$
Medium mass	4.4	1000 kg	58	0.075	180	20 k	535 B$
Large mas	12	20 ktons	12	0.70	4000	3.4	15 P$

Once the payload reaches Alpha Centauri, it takes another 4.4 years for the photos to return to Earth, so a total of 26.4 years after launch.

Based on the results of our panel at OPAL 2024, PCSELs (Phased Crystal Surface Emitting Lasers) are now seen to be the ideal photon source for these flights rather than individual CW lasers. Each 3-cm wafer can, in principle, produce 10 kW of light already phased.

When complete, these wafers will be the brightest source ever created. Please see Section 6 for more details on PCSELs.

3. Ways of Slowing Down in PPP

Parkin assumes a slowdown laser at the end of a PPP trip. But to use an extreme case, If I'm returning from an 1823 departure at a speed of 1/8 AU/minute, and I expect you to be there for me at this moment to actuate the slowing beam, good luck! Because we can't put a slowing laser at every possible destination, we need to be able to slow ourselves. There are ways of braking using the magnetic fields in space so that you don't have to have a "slowdown" beam waiting for you.

The secret is:

$$\bar{\mathbf{F}} = q\bar{\mathbf{v}}x\bar{\mathbf{B}}, \quad (16)$$

with q the (signed) charge on your spacecraft. This force will likely be perpendicular to the plane of your orbit around a star because the magnetic field is often radial.

You can control the sign and magnitude of magnetic force by choosing to emit electrons or protons. Near Earth, B = 60 μtesla so the force on a single milli- coulomb is 15N. This force will likely be perpendicular to the plane of your orbit around a star because the magnetic field is often radial.

By periodically creating that perpendicular velocity and reversing it, your kinetic energy is gradually given to the star that created the magnetic field. Of course, this option could take years and might be most suitable for instruments.

4. Existential Problem: Questions about Relativistic Human Travel

At β = 0.7, γ = 1.96, and time is advancing twice as fast for travelers as it is for people back home. At β = 0.99, γ = 7.05 and kinetic energy density is $7.05 m_o c^2$. Considering that in a thermonuclear explosion, only 0.7 % of hydrogen rest mass is converted to energy [8], at this speed, kinetic energy density is 1000 times larger than the energy density in a hydrogen bomb.

This fact makes it critical to design the system with international cooperation so that no one will think it is a weapon in disguise.

We must design our flight path with care! The cost per kg for this acceleration level is 6.26 B$ [7], Table 3. For a 100 ly trip, you can return home in 32 years, but all your friends will be 204 years older!

Would you like that? Some people would.

How many Earth-sized planets are inside the "Goldilocks zone" of temperature and also within 100 ly of Earth? Andrew McGregor [6] says, "Exactly one, and it wouldn't be very comfortable. One. It's called Gliese667 Cc." Gliese is 24 ly distant, and its gravity is twice that of Earth.

5. Practical Limits

a. Human travel at relativistic speeds requires a far different investment of emotional and financial effort than just going to the moon. I guess that, because of the incredible expense, it seems likely that human relativistic travel will not happen for a long time. And you can't go faster than the speed of light.
b. Funding. Capital plus operating expense to get a 10-tonne spacecraft to 0.99c. is 63 T$, or 6.3 B$/kg. That's $2200 for each inhabitant of Earth. On the other hand, we could afford to accelerate an 8 kg mass to 0.99c. So, this kind of technology is primarily useful for instrument packages now. Because 2530 is the presumed year of completion for this project, all that is required to launch the 10-tonne spacecraft 500 years from now is a 0.23 %/yr growth rate of the world's economy.
c. Psychological and emotional limits can be avoided if I travel with a tribe of rich people and don't intend to return. Even so, we would guess that a 15-year trip is the maximum investment of time for intelligent living beings, but very few billionaires could afford the cost.
d. Laser aperture for just the β = 0.7 example is 1800 km. Few places on Earth have so much empty land. Perhaps the laser could be put on the Moon, but that option would be very expensive.
e. Why haven't we actually seen extra-terrestrials originating within 100 lightyears of Earth in my lifetime, despite all the hype and hope? Why are no little green corpses at Area 51 in Nevada?
f. We are <u>alone</u>. The sooner we accept that and treat our civilization and its products as precious, the better. What is the chance that for advanced civilizations don't destroy themselves before traveling to us? Assume that a society which has advanced technologically to the point of making atomic weapons lasts 2000 years before self-destructing. This is a generous assumption. Assume that, like us, it takes about 4B years to evolve from slime to intelligence. Even if it's 8B years, the ratio is one in 2 million. That means that out of

2 million Earthlike exoplanets, one now has intelligent life. If intelligent beings will not want to travel further than 15 ly to find intelligent neighbors, and if there's just one planet in the Goldilocks zone in our 200 light-year diameter sphere, the chances of finding intelligent life nearby or of having it threaten us are vanishing.

6. PCSELs – Lasers for Breakthrough Starshot

6.1. Current State-of-the-art in Light Propulsion

We are still discussing and working on laser sources that could be applied for photon propulsion. Solar light is used to validate the technology. The most recent NASA experiment demonstrates a solar sail that uses light pressure acting on a large 80 m^2 reflective polymer sheet to provide propulsion for a small 12U satellite with a weight of 4.6 kg for future space missions [10].

The Breakthrough Starshot mission seeks to send a gram-scale chip satellite with a 4 m^2 light sail propelled by an Earth-based laser [11]. It is estimated that millions of kW-class lasers with an overall power of 100 GW working for 10 minutes are needed to speed up the sail to 20 % of the speed of light (0.2c). At the end of the acceleration stage, the sail will be at a distance of 15 million km. Therefore, the diffraction of the beam should be managed, requiring a kilometer-scale laser source if operating at a 1-micron wavelength. This could be achieved only by coherently combining multiple light emitters.

6.2. Progress in Laser Beam Combining

There are two main techniques for coherent laser beam combining [12]:

- Side-by-side combining a phased array of lasers, leading to a larger beam size. By synchronizing their optical phases, the joint large beam could have a reduced beam divergence;
- Filled-aperture techniques, where several beams are combined into a single beam with the same beam size and divergence, using diffraction grating or similar optical element.

Most of the experiments are made with fiber lasers. A coherent beam combining using a grating up to 5 kW laser power at 82 % efficiency was shown [13]. G. Mourou et al. [14] proposed an approach combining 30,000 phase-locked fiber lasers to achieve a 100-petawatt laser beam. The method was tested experimentally with 64 phased fibers, and a phase map was captured every ~30 ms. M. Shpakovich et al. [15] proposed the dynamic phase control of a laser beam array based on a simple neural network included in a phase correction loop. Experiments demonstrated the high performance and scalability of the scheme with an array of up to 100 laser beams and a phase setting at $\lambda/30$. A real high-power laser system should include electro-optic modulators distributed on the inputs of an amplifier array to lock the output beams on desired phase relationships. C. P. Bandutunga et al. present a photonic solution for optical phase sensing and control to enable the coherent combination of order 10^8 individual lasers, including the ability to sense and compensate for atmospheric distortions, assuming the laser system is ground-based [16]. To limit losses due to atmospheric turbulence, the laser beamer will require an adaptive optics system, and 10^8 piston-phase actuators with relevant sensing are required per square kilometer of array size.

6.3. Lasers

Various types of lasers are considered a potential choice for getting 100 GW power. Selection criteria include cost per watt, the ability of coherent combining, wall-plug efficiency, size, cooling, etc. Solid-state lasers could hardly meet cost, efficiency and size requirements. Fiber lasers look more promising, but there are challenges in upscaling the manufacturing. Their cost highly depends on the cost of laser diodes used to pump fiber lasers. Permanent progress and scaling manufacturing of laser diodes leads to a constant drop in their price. It is expected that the target price of 0.1-0.01 USD/Watt will be reached by 2040 [17].

Keeping in mind high wall-plug efficiency and direct emission of coherent light, other types of semiconductor (diode) lasers are under consideration for light sail propulsion. An array of electrically pumped vertical external cavity surface-emitting lasers (VECSELs) can be of long coherence and provide sufficient power density at 100 mW per 1 mm emitter [11]. Single-mode VECSELs with a power of 500 mW have been demonstrated at 500 mW [18]. The high areal fill factor required for efficient energy transfer to the sail could be achieved. However, it remains unclear if billions of VECSELs can be incorporated into an architecture that maintains coherence and phase over these spatial scales.

Photonic-crystal surface-emitting lasers (PCSEL) are a new promising candidate to be a building block for kilometer-sized laser arrays [4, 19].

PCSELs are single-mode semiconductor lasers capable of high power and high beam quality and can deliver a laser power of up to 1 kW from a 1 cm-sized emitter with an experimentally shown brightness of ~1 GW/cm^2/sr [20]. The authors expect to make 3-cm diameter lasers with output powers exceeding 10 kW and brightness up to 1,000 GW/cm^2/sr [21].

Even though 3-cm-sized 10 kW PCSEL lasers are still a dream, we could consider manufacturing capabilities. Ten million 10 kW PCSEL lasers are needed for the required 100 GW laser power. A 12-inch-diameter wafer could incorporate 65 lasers.

This corresponds to 155,000 12-inch wafers – a small amount compared to the annual capacity of the manufacturing facilities managed by TSMC and its subsidiaries only, which exceeded 16 million 12-inch equivalent wafers in 2023 [22]. Therefore, manufacturing this kind of laser chips would not be a problem even with today's capacities. Challenges could be in their packaging and electrical supplies. The PCSEL emitters themselves could fit into an area of 120×120 sq. meters.

However, the open question remains: Are PCSEL-type lasers easy to control by phase? How is that opportunity preserved by upscaling the single laser power?

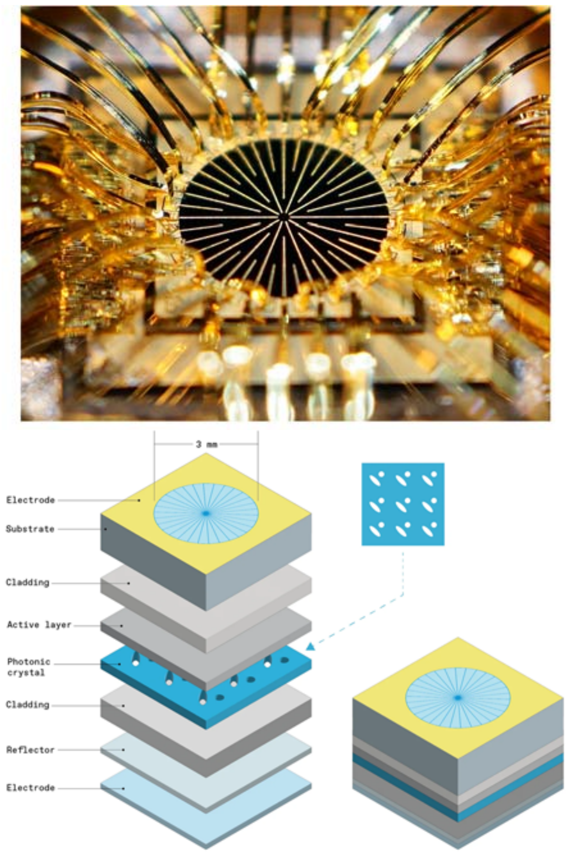

Fig. 3. Photonic-crystal surface-emitting laser [4].

7. Conclusions

- Relativistic laser space propulsion is just around the corner. Plans are underway to launch a probe to Alpha Centauri at 20 % of the speed of light using a giant CW laser;
- This probe can return at least one photo to Earth with reasonably sized apertures. The 1-meter aperture for doing that needs to be considered as part of the payload. Dr Parkin believes the lightsail itself can redirect photos to the Earth;
- The same technology can be used to launch instrument packages across the near universe.

Support for laser development is the key. As Prof. Raciukaitis pointed out in his presentation ("With Lasers to the Stars") at our panel in OPAL 2024, [8], PCSELs (Photonic Crystal Surface Emitting Laser) can have a brightness of 1GW/cm^2/sr, brighter than any laser existing today [4]. A 3 cm diameter PCSEL wafer can potentially emit 10 kW of automatically phased light. These can be phased together in a plane wavefront, or a parabolic wavefront for focusing, and such a plane wave can be instantaneously steered. This is how we can create a single 250 GW beam, such as is required for Breakthough Starshot.

Acknowledgments

For the discussion of PPP, Claude Phipps is deeply indebted to calculations by and discussions with Dr Kevin Parkin. My conclusions about PPP are more skeptical than his. Dr. Parkin firmly believes in the future of all aspects of this field, including human travel. I hope he's right. I sincerely thank Séverine Boyer, CNRS, for her support in this work.

References

[1]. C. Phipps, Laser parameters for laser ablation and photon propulsion, in *Proceedings of the 7th International Conference on Optics, Photonics and Lasers (OPAL'24)*, Palma de Mallorca, Spain, 15-17 May 2024, pp. 25-28.
[2]. S. Scharring, et al., Heat accumulation in laser-based removal of space debris, *J. AIAA*, Vol. 56, 2018, pp. 2506-2508.
[3]. C. Phipps, C. Bonnal, Preflight preparations for active debris removal and ranging, *Sensors and Transducers* Vol. 258, Issue 4, 2022, pp. 25-30.
[4]. https://spectrum/ieee.org/pcsel
[5]. K. L. G. Parkin, The breakthrough starshot system model, *Acta Astronautica.*, Vol. 152, 2018, pp. 370-384.
[6]. What are some nearby Earth-sized exoplanets around 15-30 light years away?, https://www.quora.com/What-are-some-nearby-Earth-sized-exoplanets-around-15-30-light-years-away
[7]. K. L. G. Parkin, Private communication.
[8]. Hydrogen Bomb Mass to Energy?, https://physics.stackexchange.com/questions/135013/hydrogen-bomb-mass-to-energy
[9]. G. Raciukaitis, With lasers to the Stars, *Presented at the 7th International Conference on Optics, Photonics and Lasers (OPAL'24)*, Palma de Mallorca, Spain, 15-17 May 2024 (panel discussion).
[10]. Rocket Lab launched a NanoAvionics satellite bus carrying NASA's solar sail system aboard, https://nanoavionics.com/news/
[11]. S. P Worden, et al, Progress on the Starshot laser propulsion system, *Appl. Opt.*, Vol. 60, 2021, pp. H20-H23.
[12]. Coherent Beam Combining, https://www.rp-photonics.com/coherent_beam_combining.html
[13]. R. H. Holten, A. Flores, T. Ehrenreich, B. Anderson, I. Dajani, Beam-combinable high-power fiber laser sources for directed energy applications, in

Proceedings of the High-Power Laser Ablation VIII Conference, 26 February – 1 March 2024, Santa Fe, NM, USA, p. 12939-30.

[14]. G. Mourou, B. Brocklesby, T. Tajima, J. Limpert, The future is fibre accelerators, *Nature Photon*, Vol. 7, 2013, pp. 258-261.

[15]. M. Shpakovych, G. Maulion, V. Kermene, A. Boju, P. Armand, A. Desfarges-Berthelemot, A. Barthelemy, Experimental phase control of a 100-laser beam array with quasi-reinforcement learning of a neural network in an error reduction loop, *Optics Express*, Vol. 29, Issue 8, 2021, pp. 12307-12318.

[16]. C. P. Bandutunga, P. G. Sibley, M. J. Ireland, R. L. Ward, Photonic solution to phase sensing and control for light-based interstellar propulsion, *Journal of the Optical Society of America B*, Vol. 38, Issue 5, 2021, pp. 1477-1486.

[17]. R. J. Deri, Semiconductor Laser Diode Pumps for Inertial Fusion Energy Lasers, LLNL-TR-465931, 1018822, *Lawrence Livermore National Laboratory*, 2011.

[18]. J. G. McInerney, Evolution of the Novalux extended cavity surface-emitting semiconductor laser (NECSEL), *Proceedings of SPIE*, Vol. 9734, 2016, 973403.

[19]. S. Noda, K. Kitamura, T. Okino, D. Yasuda, Y. Tanaka, Photonic-crystal surface-emitting lasers: Review and introduction of modulated-photonic crystals, *IEEE J. Sel. Top. Quantum Electron.*, Vol. 23, Issue 6, 2017, 2696883.

[20]. T. Inoue, M. Yoshida, J. Gelleta, K. Izumi, K. Yoshida, K. Ishizaki, M. De Zoysa, S. Noda, General recipe to realize photonic-crystal surface-emitting lasers with 100-W-to-1-kW single-mode operation, *Nature Comm.*, Vol. 13, 2022, 3262.

[21]. S. Noda, M._Yoshida, T. Inoue, The Tiny Ultrabright Laser that Can Melt Steel, https://spectrum.ieee.org/u/takuya-inoue

[22]. Fab Capacity, https://www.tsmc.com/english/dedicatedFoundry/manufacturing/fab_capacity

Sensors & Transducers, Vol. 266, Issue 3, August 2024, pp. 16-24

Sensors & Transducers
Published by IFSA Publishing, S. L., 2024
http://www.sensorsportal.com

Thin-film Interference Demultiplexer for VIS-WDM

[*] Ulrich H. P. FISCHER and Mladen JONČIĆ
Harz University of Applied Sciences, 38855 Wernigerode, Germany
Tel.: +49 152 5363 5589
[*] E-mail: ufischer@hs-harz.de

Received: 24 April 2024 / Revised: 3 July 2024 / Accepted: 5 August 20204 / Published: 12 April 2024

Abstract: In short-range communication 1 mm PMMA Step Index Polymeric Optical Fibers established itself as a reasonable. alternative to the traditional data communication media such as glass fibers, copper cables and wireless systems. Due to multiple advantages such as a large core diameter, tolerance to fiber facet damages and low installation costs, the SI-POF is typically used for network systems in homes, vehicles and industrial automation. For wavelength division multiplex an optical demultiplexer is a key component. The paper concentrates on the demultiplexing techniques employing thin-film interference filters used in Polymeric Fiber Transmission Systems. An interference filter-based Step Index Polymeric Optical Fibers demultiplexer was realized using a precisely adjustable. opto-mechanical setup, which allowed maximization of the optical throughput in the individual channels. Intermediate setups with two and three channels were first established. In addition, a serial and a two-stage configuration of a target setup with four channels were realized. It was shown that the latter configuration outperformed the former one in terms of Insertion Loss (IL) and IL uniformity. Furthermore, the demultiplexer with two-stage configuration provided low insertion loss (< 5.7 dB) and high channel isolation (> 30 dB). It outperformed other interference filter- based SI-POF demultiplexers reported so far, and was well suited for implementation in high- speed POF WDM transmission experiments. To demonstrate experimentally the feasibility and potential of a high-speed POF WDM concept, a four-channel data transmission setup was realized.

Keywords: Polymeric fiber transmission systems, WDM transmission, Interference demultiplexer, POF-multiplexer.

1. Introduction

Polymeric Optical Fibers (POF) is very attractive for the use in short-range telecommunication networks. Among different types of POF, the standard 1-mm diameter Step Index-POF is the best known and by far the most widely used type of POF. SI-POF offers many advantages in comparison to alternative data communication media such as glass fibers, copper cTab.s, and wireless systems. It is pliTab., durTab., and inexpensive, offers small weight and short bend radius, allows easy installation and quick troubleshooting, and also provides the immunity to electromagnetic interference. Due to its numerous advantages SI-POF is already applied in various application sectors (in-house networks, automotive and aerospace industry, industrial control, etc.) [1].

Present communication systems over POF use a single channel for data transmission. Commercial systems with SI-POF can deliver a bandwidth of 250 Mbit/s over 50-100 m. Multi-Gbit/s transmission over SI-POF was demonstrated in the laboratory conditions [2]. However, the standard SI-POF has the lowest capacity among all POFs due to the strong inter-modal dispersion and high attenuation [3].

To increase the capacity of a single POF, multiple optical carriers can be used for parallel transmission of communication channels over the same fiber. The technique is known as Wavelength Division Multiplex (WDM). In glass fiber communications WDM has already been firmly established for two decades, and represents the key technology in modern long- and medium-haul optical communication systems [4].

A growing interest to develop WDM components and systems for POF is present in recent years [5]. WDM technology for POF is already under investigation by several working groups [6-8]. The development of the key WDM components (e.g.

DEMUX: Demultiplexer, MUX: Multiplexer) (Fig. 1) is essential to the success of WDM over POF. It is also important to define a unique set of WDM transmission channels for the realization of standardized commercial WDM devices and systems for POF. A principle of an WDM structure is depicted in Fig. 1.

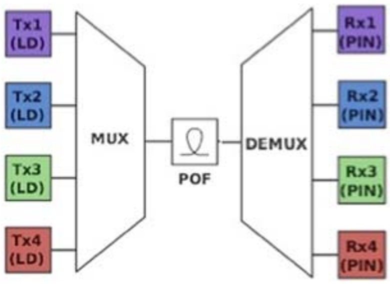

Fig. 1. Basic structure of an optical four-channel WDM transmission system over POF with its components.

In [9, 10] the extension of *Coarse* WDM grid (according to ITU-T G.694.2 Rec. [11] into the visible spectrum was proposed as a spectral grid for CWDM applications over SI-POF in [9].

The working group at the Harz University is working about the key-components for high-speed communication over POF, especially optical MUX/DEMUX element, are researched and developed in the project HOPE (*High Speed Optical Transmission Systems using Polymeric Fibers*) of the German Federal Ministry of Research [12]. One goal of this project is the realization of a low-cost grating based DEMUX in injection molding technology [13, 14]. Another goal of the project is the investigation and realization of a 10 Gbit/s four-channel CWDM transmission system over 50 m SI-POF link using interference filters. Course WDM in the visible region of our experiment means channel spacings of 20 nm – 100 nm.

2. Transmission Properties of 1 mm PMMA SI-POF

The 1 mm PMMA SI-POF is the best known and by far the most widely employed type of POF. It is made of 980 µm diameter PMMA core surrounded by a thin cladding (10 µm) made of fluorinated polymer. The typical spectral attenuation of SI-POF is shown in Fig. 2. The fiber supports operation in the visible spectrum from 400 nm to 700 nm. The lower wavelength bound is determined by the degradation of the PMMA compound with prolonged exposure to the ultraviolet (UV) wavelengths [15]. The attenuation value of around 400-450 dB/km, that still allows operation over shorter link lengths (< 20 m), sets the upper wavelength bound.

Two intrinsic loss mechanisms contribute to the raise of attenuation at shorter and particularly UV wavelengths. The electronic transitions due to the absorption of light in the polymer compound cause absorption peaks in the UV region. However, their absorption tails extend through the visible spectrum affecting the POF attenuation [16]. The dependence of the attenuation coefficient of electronic transitions α_e [dB/km] on the wavelength for PMMA is given by [17]:

$$\alpha_e = 1.58 \cdot 10^{-12} exp\left(\frac{1.15 \cdot 10^4}{\lambda}\right) \quad (1)$$

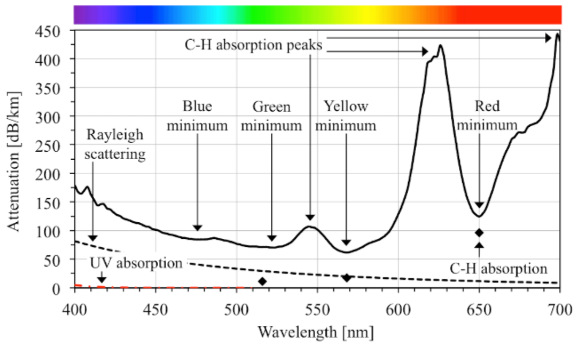

Fig. 2. Typical spectral attenuation of 1 mm PMMA SI-POF [18] with contributions of intrinsic loss mechanisms and with attenuation minima and maxima.

The second loss mechanism is the Rayleigh scattering. It is caused by the structural irregularities in the polymer compound that are much smaller than the wavelength of light (order of one tenth of wavelength or less). The effect of scattering becomes more pronounced as the wavelength decreases since the scattering attenuation coefficient α_s [dB/km] is inversely proportional to the fourth power of the wavelength [19]:

$$\alpha_s = 13 \cdot \left(\frac{633}{\lambda}\right)^4 \quad (2)$$

In the infrared region the attenuation significantly increases due to the intrinsic absorption losses caused by vibrations of the molecular C-H bonds (total of eight per MMA monomer). The higher overtones of the C-H bond vibrations also extend in the visible spectrum. The 7th overtone at 549 nm, and particularly the 6th and the 5th overtone at 627 nm and 736 nm respectively, cause pronounced absorption peaks and wide absorption bands, predominantly determining the level of attenuation in the red spectral range [20, 21].

The contributions of the intrinsic loss mechanisms to the overall attenuation of SI-POF are also shown in Fig. 2. The attenuation contributions due to the vibrations of C-H bonds at 516 nm, 568 nm and 650 nm are taken from [19]. The sum of individual intrinsic loss mechanisms corresponds to the theoretical loss limit and equals approx. 40 dB/km, 37 dB/km and 107 dB/km at the respective wavelengths. In practice is this limit never achieved due to the extrinsic loss processes (absorption due to impurities in the fiber core, scattering loss due to waveguide structural imperfections, etc.) [16].

The wavelength regions where the fiber exhibits low attenuation are called attenuation windows. The SI-POF has four attenuation windows. Those are blue, green, yellow and red windows, with the absolute attenuation minimum of approx. 62 dB/km at around 568 nm (yellow window). The parameters of the attenuation windows are listed in Table 1.

Table 1. Attenuation windows of SI-POF (based on the attenuation curve from Fig. 2.

Attenuation window	blue	green	yellow	red
Attenuation minimum [dB/km]	85	70	62	125
Wavelength of the attenuation minimum [nm]	476	522	568	650
Approximate 3 dB width of the window [nm]	19	24	8	4

The mean refractive index of SI-POF core material in the visible spectrum is n_{core} = 1.492, whereas the refractive index of cladding is n_{clad} = 1.412. Due to the big difference in refractive indices of core and cladding, the numerical aperture (NA)

$$NA = \sqrt{n_{core}^2 - n_{clad}^2} \quad (3)$$

has the value of 0.482 (usually rounded to 0.5). The corresponding maximum acceptance angle of the fiber is 30º. The large core radius a_{core} = 490 µm combined with the high NA results in the normalized frequency V:

$$V = 2\pi \frac{a_{core}}{\lambda} \cdot NA \quad (4)$$

of 2698 at 550 nm, which is far above the limit V = 2.405 below which a fiber is single-moded. The number of modes N_{mod} propagating through SI-POF can be approximated as

$$N_{mod} \approx V^2/2, \quad (5)$$

corresponding to 3.64 million modes at 550 nm. Due to the significant path difference between lower and higher order modes, propagating respectively at smaller and larger angles relative to the optical axis, the strong intermodal dispersion is inherent to SI-POF. In the time domain it is manifested as pulse broadening, thus introducing the inter-symbol interference (ISI). In the frequency domain the intermodal dispersion results in a low pass frequency response, constraining the bandwidth-length product of SI-POF to around 50 MHz × 100 m [22].

3. Demultiplexing for 1 mm PMMA SI-POF

The WDM is one possibility to increase the data carrying capacity of SI-POF. The key component for WDM is a wavelength demultiplexer. Different approaches for realization of the demultiplexer for SI-POF have been investigated, including demultiplexing based on a dispersion prism, thin-film interference filters, and a diffraction grating (plane or concave).

The prism-based two-channel demultiplexer operating with LEDs at 530 nm and 650 nm was reported in [23]. The insertion loss (IL) and the crosstalk were around 17-20 dB and -20 dB respectively. Another solution employing the dispersion prism was shown in [24]. The three-channel demultiplexer operated with LEDs at 470 nm, 520 nm and 650 nm. It provided the IL of 12-20 dB, whereas the crosstalk took values between -4.6 dB and -34.8 dB. High IL and considerable crosstalk were caused by unoptimized optical components, broad LED spectra and high alignment sensitivity of both setups.

The two other demultiplexing techniques have been recognized as the most promising for SI-POF and have been the most investigated so far. This work focuses on the demultiplexers employing interference filters.

3.1. Demultiplexing Employing Thin-film Interference Filters

The technology based on thin-film interference filters is mature and one of the most commonly applied technologies for realization of WDM demultiplexers in single-mode glass fiber communication. The demultiplexers for *Coarse* WDM applications cascade the interference filters to provide up to 16 flat-top channels between 1271 nm and 1611 nm, with 20 nm minimum channel spacing [25]. The typical parameters of commercial 4-, 8-, and 16-channel demultiplexers with IL less than 1.6 dB, 2.7 dB and 3.7 dB respectively, can be found in [26]. The thin-film filter-based demultiplexers for *Dense* WDM applications are commercially available. with up to 40 channels in 1550 nm region and less than 8 dB IL. Instead of simply cascading the filters, those devices usually employ a modular configuration described in [27]. The same reference provides a typical transfer function of the 40-channel demultiplexer with 3-6 dB IL and 100 GHz (0.8 nm) channel spacing.

In the visible spectrum, and thus within the application range of SI-POF, a vast variety of thin-film interference filters is available from various manufacturers. Even though not particularly intended for POF applications, the visible interference filters represent an attractive solution for POF demultiplexers, where wavelength selectivity, low IL and high isolation are required.

An interference filter, typically designed for 0º angle of incidence (AOI), utilizes the principle of constructive and destructive interference to selectively transmit certain wavelengths and reject (diminish in intensity and reflect) the others [28]. Its basic structure comprises multiple thin dielectric layers with alternating high and low refractive indices, which are successively deposited on a single glass substrate. The desired spectral response is obtained by a careful selection of the number of dielectric layers, their thickness and refractive indices. The filter is typically characterized with high passband transmittance (> 90 %), steep transition slopes (> 3 dB/nm) and deep blocking (> 30 dB) in rejection bands (see Fig. 3).

Table 2. Basic parameters of hard-coated bandpass interference filters from Edmund Optics utilized in different demultiplexer setups (datasheet information).

Center wavelength [nm]	405	450	525	640	650	660
3 dB passband bandwidth [nm]	10	10	50	10	50	10

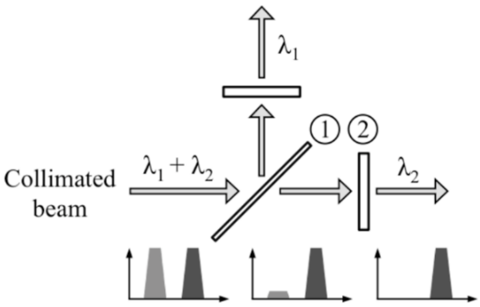

Fig. 3. Principle of separation of two collimated wavelength channels employing thin-film interference filters: 1 is the dichroic mirror (45º AOI); 2 is the interference filter (0º AOI).

A dichroic mirror is a special type of interference filter intended for the spatial separation or combination of light at different wavelengths. It is designed to operate at 45º AOI, such that a certain spectral range is transmitted, whereas the rejected wavelength range is reflected at 90º angle with respect to the incident optical axis. A commercial visible spectrum dichroic mirror has a transition slope between the transmission and reflection band of typically 30-40 nm (see Figs. 4, 5 and Table 3).

This is significantly less steep compared to the standard interference filters designed for the normal incidence. Unlike an interference filter, e.g. a long pass mirror must be not only highly transmissive above the cutoff wavelength, but also highly reflective below it. Therefore, producing steeper slopes would require increased complexity of the coating, and accordingly, a significant rise in production costs.

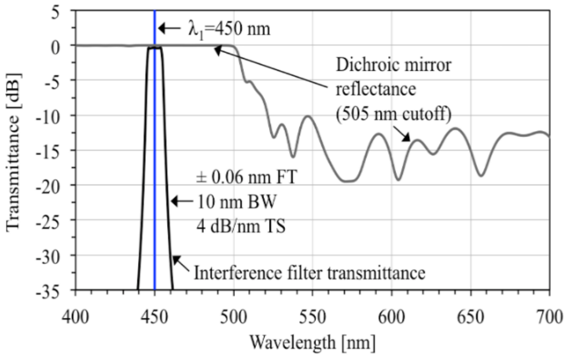

Fig. 4. Selection of the dichroic mirror and interference filters for demultiplexing two wavelength channels centered around λ_1 = 450 nm.

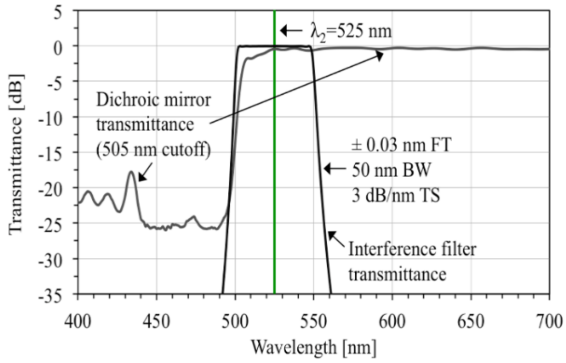

Fig. 5. Selection of the dichroic mirror and interference filters for demultiplexing two wavelength channels centered around λ_2 = 525 nm.

Table 3. Basic parameters of hard-coated dichroic mirrors utilized in different demultiplexer setups (datasheet information).

Type		Long-pass		Short-pass
Cutoff wavelength [nm]	425	505	567	650
Transmission band [nm] (> 85 %)	440-700	520-700	584-700	400-630
Reflection band [nm] (> 90 %)	380-410	380-490	380-550	675-850
Manufacturer	Thorlabs	Edmund Optics		

The interference filters show significant angular dependence of their transmission characteristic [29]. To be applicable for SI-POF, the highly divergent beam from the fiber must be transformed into a bundle of parallel rays prior to the incidence. The principle of separation of two collimated wavelength channels using a dichroic mirror is shown in Fig. 1. To increase the channel isolation, an additional bandpass filtering in each of the output channels should be implemented prior to the focusing of light. As an example, a selection of the dichroic mirror and interference filters for demultiplexing two wavelength channels centered around λ_1 = 450 nm and λ_2 = 525 nm is shown in Figs. 4 and 5.

There were several attempts to realize an SI-POF demultiplexer with interference filters. The three-channel demultiplexer for the blue, green and red wavelength regions, shown in [30] offered the IL of 7-10 dB. Another three-channel solution with wide channel passbands in the violet, green and red spectral regions was reported in [31]. The device provided the IL of 6-7 dB and high channel isolation. By far the best three-channel demultiplexer was reported in [32]. It had wide (> 50 nm) channel passbands in the violet/blue, green and red spectral regions, the IL as low as 2.5 dB (at 570 nm), and high isolation between the channels (> 30 dB). At 450 nm, 520 nm and around 650 nm (lasing wavelengths used for SI-POF communication and in this thesis) the IL was 5 dB, 3 dB and 3 dB respectively. The demultiplexer offered small dimensions by employing a plastic housing with slits for lenses and dichroic mirrors. Furthermore, it allowed easy connection of the input and the output fibers to the housing.

In the patent [33] the same authors as in [34] proposed the design of a four-channel demultiplexer by cascading the dichroic mirrors. To the best of author's knowledge, no information about practical realization of the setup has ever been published. The only four-channel demultiplexer realized so far was shown in [35]. It was based on a two-stage configuration and operated with LEDs at 470 nm, 520 nm, 590 nm and 650 nm. The IL of the setup was estimated to be 4-5 dB, but no transfer function was provided by the author. Since no additional filtering was implemented in the output ports, the demultiplexer experienced very high crosstalk. Therefore, it could not be used as a stand-alone component, but rather in combination with an electronic crosstalk compensation.

When properly designed, an interference filter-based demultiplexer is capable. of providing low IL and high isolation. That makes it suitable. for realizing and investigating POF WDM communication systems. In the thesis this demultiplexing approach for SI-POF is further investigated. The goal is to increase the channel count compared to [30, 36] and [34], and realize a four-channel demultiplexer with improved performances compared to [35].

4. Key WDM Components

The realization of high-speed POF WDM systems requires high-speed high-power visible LDs. Recent development progress brought to the market different violet, blue, green, and red LDs. A wavelength MUX and DEMUX for the visible spectrum are indispensable photonic components in a CWDystem under development. These have been recently realized at the Harz University. In this section, we give an overview of acquired LDs. In addition, developed MUX and DEMUX are presented in [37].

4.1. Laser Diodes

The basic parameters of LDs used in our WDM system are listed in Table 4 and shown in Figs. 6 and 7 The commercially available LDs at 405 nm, 450 nm, and 639 nm operate in WDM channels 1, 2, and 4 respectively. The 514 nm research and development sample is assigned to channel 3.

Table 4. Parameters of Laser Diodes used in WDM system.

MUX input port / WDM channel	1	2	3	4
Launching coupling loss + 400-µm fiber attenuation [dB]	4.89	4.93	4.63	4.56
Connector loss [dB]	0.1	0.58	0.22	0.3
Total loss [dB]	4.99	5.51	4.85	4.86

Fig. 6. LD soldered to a formable coax cable.

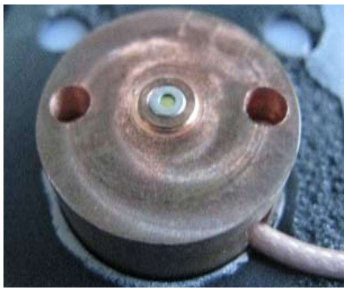

Fig. 7. LD mounted in a copper retainer ring.

4.2. Multiplexer

POF couplers can be used to efficiently combine signals with different wavelengths onto a single fiber. The multiplexing function of a 4:1 coupler is shown in Figs. 8, 9 and 10.

To multiplex the output beams of the LDs, a simple 4:1 POF coupler has been realized with commercially available components. Four 60 cm long 400-µm diameter PMMA SI-POFs with installed 400-µm diameter FC connectors were used as the input ports. The LDs were butt-coupled to these fibers by means of a coupling unit. On the link side, the 400-µm fibers were glued together in a standard 1-mm diameter FC connector to form the MUX output port at the connector end face.

To connect the MUX output port to the 1-mm diameter SI-POF link, a simple FC connector coupling was used with index matching gel between the connector end faces.

To optimize the MUX design, a 970-µm diameter FC connector should be used at the output port. The mechanical and optical set-up is depicted in Figs. 9 and 10.

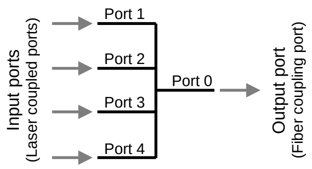

Fig. 8. Multiplexing function of 4:1 coupler.

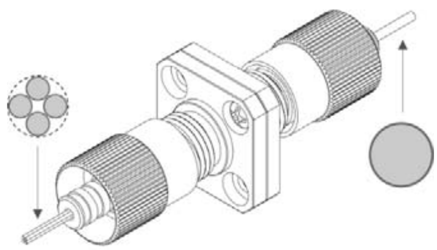

Fig. 9. Four-legged multiplexing POF bundle set-up with FC connector.

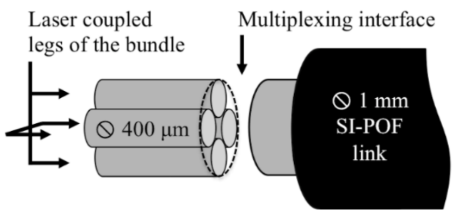

Fig. 10. Cross section of 4 400 µm fibers and 1 mm fiber.

The insertion loss (IL) of the MUX, consisting of launching coupling loss, 400-µm fiber attenuation, and connector loss, is given in Table 5.

Table 5. Insertion loss of the MUX.

WDM channel	1	2	3	4
Emission wavelength [nm]	405	450	514	639
Opt. output power [dBm]	16	19	17	10
Threshold current [mA]	35	30	60	30
Operating current [mA]	70	100	160	40

4.3. Demultiplexer

Different proposals for the realization of the DEMUX for SI-POF have been reported in the past. Except one (four-channel), all of the realized DEMUXs were two-channel or three-channel solutions. A good overview of these proposals can be found in [3, 10, 8, 13]. Three main approaches for DEMUX realization were prism-based, filter-based, and grating-based DEMUX.

A four-channel filter-based DEMUX has been realized in the bulk optics technology at the Harz University. The principle of operation of the DEMUX is shown in Fig. 11. A multi-wavelength light beam exiting the sending fiber end face is first collimated by means of an aspheric lens. Dichroic mirrors used in the DEMUX are designed for the use at a 45° angle of incidence. The first dichroic mirror (colored orange) reflects violet and blue while transmitting green and red spectral portion of the incidence light beam. The second dichroic mirror (colored blue) reflects violet while transmitting blue, and the third dichroic mirror (colored red) reflects green while transmitting red spectral portion of the incidence light beam. Interference filter is placed in each channel to reduce the crosstalk and to narrow the channel passband. Filtered light beam is then focused on the receiving fiber end face by means of an aspheric lens, and fed to the receiver.

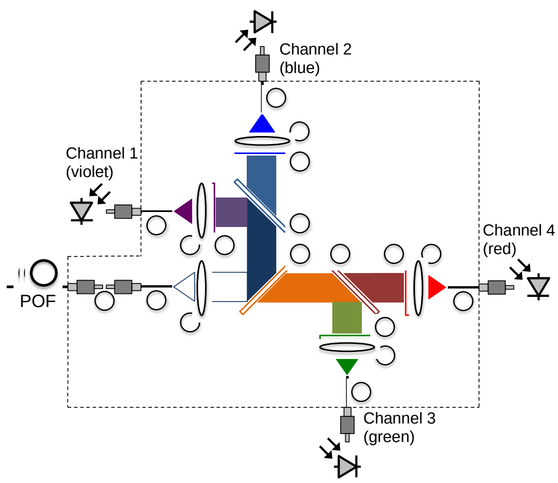

Fig. 11. Principle of operation of a four-channel DEMUX: 1 is the FC connector coupling; 2 is the 1 m SI-POF; 3 is the aspheric lens; 4 is the dichroic mirror; 5 is the interference filter.

The basic DEMUX parameters are summarized in Table 6.

The realized DEMUX supports the spectral grid proposed in [6, 7, 9] by showing that it is possible to realize channels with narrow passbands (< 10 nm).

To the best of author's knowledge, high number of channels, low IL, and high isolation make this DEMUX the best DEMUX solution for SI-POF reported so far.

The fiber coupled power, the power at the output of the 25 m SI-POF link and the received power at DEMUX output ports are shown in Table 7 and the spectrum in Fig. 12 received powers comply with the recommended maximum input optical power for

SPD-2 photoreceiver of -4 dBm. To maximize the modulation amplitude and thus the signal-to-noise ratio of the modulating signal, the longitudinal offset was introduced between the LDs and the input ports of the MUX in order to reduce the coupling efficiency and not exceed the -4 dBm limit at the receiver.

Table 6. Basic DEMUX parameters.

DEMUX channel	1	2	3	4
Center wavelength [nm]	404.9	450.1	528.3	646.4
3 dB passband bandwidth [nm]	9.5	9.4	41.6	47.6
IL [dB]	5.66	4.55	3.47	3.19
IL uniformity [dB]	2.47			
Adjacent / non-adjacent channel isolation [dB]	> 30			

Table 7. Optical power levels along CWDM link.

WDM channel	1	2	3	4
Fiber coupled power [dBm]	4.49	2.36	1.76	5.58
Power at the output of the fiber link [dBm]	1.51	0.60	0.35	-0.04
Power at the output of DEMUX [dBm]	-4.00	-4.03	-4.12	-3.95

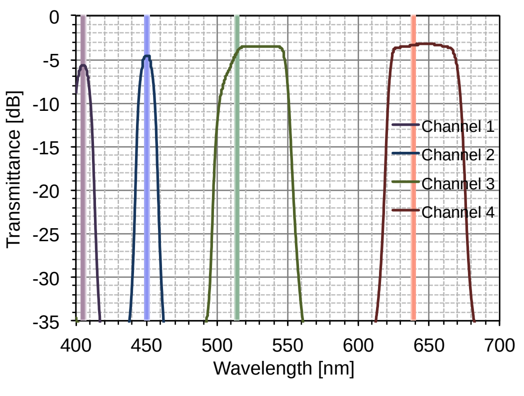

Fig. 12. Transfer function of developed four-channel DEMUX. Per channel includes the loss of one connector coupling, the loss of the opto-mechanical setup, and the attenuation of 2 m SI-POF. Lasing wavelengths indicated with colored vertical lines.

The IL of DEMUX at the lasing wavelengths can be calculated from Table 8 as the difference between the power at the output of the fiber link and the received power at the output of DEMUX. Table 5 gives the comparison of IL of DEMUX when it is estimated based on the transfer function and directly measured after 25 m fiber link. The absolute value of the difference does not exceed 0.55 dB, verifying the demultiplexing function when operating with LDs. It can be also noticed that the IL uniformity at the lasing wavelengths reduces from 2.3 dB for estimation based on the transfer function to 1.6 dB for LD launching.

Table 8. Comparison of IL of DEMUX at the lasing wavelengths.

MUX channel	1	2	3	4
Lasing wavelength [nm]	405	450	514	639
IL estimated based on the transfer function [dB]	5.66	4.56	4.15	3.36
Measured IL after MUX and 25 m SI-POF [dB]	5.51	4.63	4.47	3.91
Δ IL [dB]	-0.15	0.07	0.32	0.55

5. Data Transmission Setup

The experimental setup for the investigation of four-channel CWDM systems over SI-POF is shown in Fig. 13. It is based on the offline processing approach since no commercial components are so far available. A four-channel Agilent M8190A arbitrary waveform generator (AWG) with 12-bit vertical resolution and up to 12 GSa/s sampling rate was used to convert digital data into an analog electrical signal. In the transmission experiment, the AWG generated four independent NRZ data streams with Pseudorandom Binary Sequence PRBS test pattern length of 2^7-1 and up to 1 V_{pp} modulation amplitude.

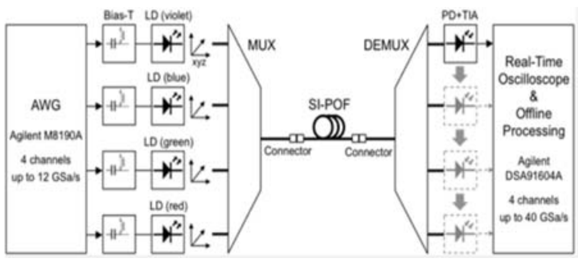

Fig. 13. Data transmission Setup with 25 m transmission.

The LDs were directly modulated in their linear lasing region with a modulation index of approximately 0.95. The optical link contained a MUX, 25 m standard SI-POF, and a DEMUX. A Graviton SPD-2 photoreceiver with a 1.2 GHz bandwidth was used for detection. As indicated in Fig. 13 the detection was performed channel after channel. Received signals were acquired by the Agilent DSA91604A real-time oscilloscope that has up to 80 GSa/s sampling rate and 8-bit vertical resolution. Further digital processing was carried out in the offline mode by means of the oscilloscope's built-in software. The equalization was performed by Serial Data Equalization software. In the experiments Feed-Forward Equalization (FFE) was used and the equalized eyes were displayed on the oscilloscope's screen for further analysis. The Bit Error Rate BER was calculated based on the quality factor or Q-factor [15], shown in Figs. 14 and 15.

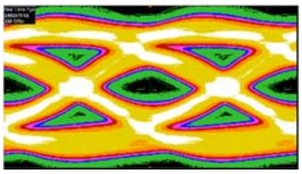

Fig. 14. Example 1 of measured eye diagram of Channel 3: at R_{b3} = 2.6 Gbit/s with Q-factor of 3.668 resulting in BER = $1.22 \cdot 10^{-4}$.

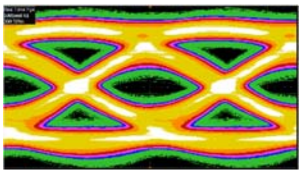

Fig. 15. Example 2 of measured eye diagram of Channel 4 at R_{b4} = 3.5 Gbit/s with Q-factor of 4.058 resulting in BER = $2.48 \cdot 10^{-5}$.

5.1. Experimental Results

The reason for different values lies in the fact that different optical sources were used in these two measurements (white light source versus LDs).

A total bit rate of 10.7 Gbit/s was transmitted over four channels.

6. Conclusions

A growing interest and activities to develop WDM components and systems for POF are present in recent years. The development of cheap and fast optical transceivers and cheap photonic WDM components is essential to the success of WDM over POF.

The current development status of a four-channel CWDM transmission system for the investigation of multi-Gbit/s data links over SI-POF is reported in the paper. The key photonic WDM components were realized at the Harz University. For combining the optical signals coming from violet, blue, green, and red LDs onto 1-mm SI-POF a 4:1 coupler with low IL was developed. A four-channel DEMUX with low IL and high isolation was realized in the bulk optics technology. To the best of author's knowledge, high number of channels, low IL, and high isolation make this DEMUX the best DEMUX solution for SI-POF reported so far. We demonstrate a 10.7 Gbit/s four-channel WDM transmission over 25 m SI-POF link at BER of less than 10^{-3}.

References

[1]. U. H. P. Fischer, M. Haupt, M. Joncic, Optical transmission systems using polymeric fibers, Chapter 22, in Optoelectronics – Devices and Applcations (P. Predeep, Ed.), *Intech Open*, 2011.

[2]. R. Caspary, *et al.*, High speed WDM transmission on standard polymer optical fibers, in *Proceedings of the 17th International Conference on Transparent Optical Networks (ICTON'15)*, 2015, pp. 1-4.

[3]. O. Ziemann, J. Krauser, P. E. Zamzow, POF Handbook - Optical Short Range Transmission Systems, *Springer Verlag*, Berlin, Heidelberg, 2008.

[4]. B. Mukherjee, Optical WDM Networks, *Springer*, Berlin, Heidelberg, 2006.

[5]. O. Ziemann, S. Loquai, J. Vinogradov, R. Kruglov, The 1 gigabit over 1 mm POF story – From vision to standard, in *Proceedings of the European Conference on Optical Communication (ECOC'10)*, Vols. 1-2, 2010.

[6]. M. Joncic, M. Haupt, U. Fischer, WDM over SI-POF – a general concept, in *Proceedings of the 13. Nachwuchswissenschaftlerkonferenz mitteldeutscher Fachhochschulen*, 2012, pp. 256-261.

[7]. L. V. Bartkiv, Y. V. Bobitski, H. Poisel, Use of concave VLS grating for combining and separating of wavelength channels in POF systems, in *Proceedings of the International Conference Modern Problems of Radio Engineering, Telecommunications and Computer Science*, 2004, pp. 2-3.

[8]. R. Kruglov, J. Vinogradov, O. Ziemann, S. Loquai, C.-A. Bunge, L. Bartkiv, Potential of CWDM technology for 10 Gbit/s data transmission over SI-POF, in *Proceedings of the Intern. POF Conference*, 2012, pp. 290-295.

[9]. J. Mladen, *et al.*, Standardization proposal for spectral grid for Vis Wdm applications over Si-Pof, in *Proceedings of the 21th Int. Conference Plast. Opt. Fibers*, 2012, pp. 351-355.

[10]. M. Jon, M. Haupt, U. H. P. Fischer, M. Joncic, M. Haupt, U. H. P. Fischer, Investigation on spectral grids for VIS WDM applications over SI-POF Untersuchung von Spektralen Gittern für VIS WDM-Anwendungen über SI-POF, in *Proceedings of the ITG Fachtagung "Photonische Netze 2013" Conference*, 2014, 38855.

[11]. I.-T. G.694.2, Spectral grids for WDM applications: CWDM wavelength grid, *International Telecommunication Union*, 2002.

[12]. U. H. P. Fischer-Hirchert, *et al.*, High-speed optical in-house networks using polymeric fibers, in Broadband Communications Networks – Recent Advances and Lessons from Practice (A. Haidine, A. Aqqal, Eds.), *IntechOpen*, 2017.

[13]. M. Haupt, Wellenlängenmultiplex im sichtbaren Spektrum für optische Polymerfaser-Systeme, *Cuvillier Verlag*, Göttingen, 2010.

[14]. S. Holl, *et al.*, Injection molding of a WDM system for POF communication, in *Proceedings of the Electronic Components and Technology Conference (ECTC'13),* 2013, pp. 2292-2297.

[15]. N. Lekishvili, L. Nadareishvili, G. Zaikov, Polymers and Polymeric Materials for Fiber and Gradient Optics, *Brill Academic Publishers*, 2002.

[16]. J. Zubia, J. Arrue, Plastic optical fibers: An introduction to their technological processes and applications, *Opt. Fiber Technol.*, Vol. 7, Issue 2, 2001, pp. 101-140.

[17]. Y. Koike, Fundamentals of Plastic Optical Fibers, *Wiley and Sons Inc*., 2014.
[18]. C.-A. Bunge, Private communication – Spectral Atenuation of Asahi Fiber Specified for MOST.
[19]. T. Kaino, Organic Molecular Solids: Properties and Applications, *CRC Press*, 1997.
[20]. C. Emslie, Review polymer optical fibers, *J. Mater. Sci.*, Vol. 23, 1988, pp. 2281-2293.
[21]. W. Groh, Overtone absorbtion in macromolecules for polymer optical fibers, *Die Makromol. Chemie*, Vol. 189, Issue 12, 1988, pp. 2861-2874.
[22]. M. Haupt, U. H. P. Fischer, Multi-colored WDM over POF system for triple-play, *Proceedings of SPIE*, Vol. 6992, 2008, 699213.
[23]. Y. Zhang, *et al.*, Study on coarse wavelength division multiplexing using polymer optical fiber transmission window, *Proceedings of the SPIE,* Vol. 5644, 2005, pp. 835-839.
[24]. U. H. P. Fischer, *et al.*, Demultiplexsystem für optische Datenübertragung mittels polymeroptischer Datenübertragung, in *Proceedings of the Nachwuchswissenschaftler Konferenz*, 2008.
[25]. H.-J. Thiele, M. Nebeling, Coarse Wavelength Division Multiplexing: Technologies and Applications, *CRC Press*, 2007.
[26]. , Product specification, 4, 8, and 16 Channel Extended Band CWDM Mux/Demux, *Lightel*, 2014.
[27]. A. K. Dutta, Dutta N K, M. Fujiwara, WDM Technologies: Passive Optical Components, *Acadamic Press*, 2003.
[28]. H. A. Macleod, Thin Film Optical Filters, 4th Ed., *CRC Press*, Taylor and Francis Group, 2010.
[29]. V. Herbert, Wavelength Filters in Fibre Optics, *Springer*, Berlin, Heidelberg, 2006.
[30]. L. V. Bartkiv, H. Poisel, A 3-channel POF-WDM system for transmission of VGA signals, in *Proceedings of the 12th International Conference on Plastic Optical Fibers*, 2003, pp. 264-270.
[31]. R. Kruglov, J. Vinogradov, O. Ziemann, S. Loquai, J. Müller, U. Strauß, C.-A. Bunge, Eye-safe data transmission of 1.25 Gbit/s over 100-m SI-POF using green laser diode, *IEEE Photonics Technol. Lett.*, Vol. 24, Issue 3, 2012, pp. 167-169.
[32]. S. Junger, W. Tschekalinskij, N. Weber, POF WDM transmission system for multimedia data, in *Proceedings of the 11th International Conference on Plastic Optical Fibers,* 2002, pp. 69-71.
[33]. W. Tschekalinskij, S. Junger, Optical multiplexer and demultiplexer for optical fibers with a large numerical aperture, European Patent, EP 1 532 477 B1, European Patent Office, 2010.
[34]. S. Junger, W. Tschekalinskij, N. Weber, POF WDM transmission system for multimedia data, in *Proceedings of the 11th International Conference on Plastic Optical Fibers,* 2002, pp. 69-71.
[35]. V. Appelt, J. Vinogradov, Simple FEXT compensation in LED based POF-WDM systems, in *Proceedings of the 11th International Conference on Plastic Optical Fibers,* 2002, pp. 127-129.
[36]. R. Kruglov, J. Vinogradov, O. Ziemann, S. Loquai, C.-A. Bunge, 10.7-Gb/s discrete multitone transmission over 50 m SI-POF based on WDM technology, *IEEE Photonics Technol. Lett.*, Vol. 24, Issue 18, 2012, pp. 1632-1634.
[37]. U. H. P. Fischer, M. Jončić, Wavelength division demultiplexer employing thin-film interference filters for the visible range, in *Proceedings of the 7th International Conference on Optics, Photonics and Lasers (OPAL'24)*, 2024, pp. 14-18.

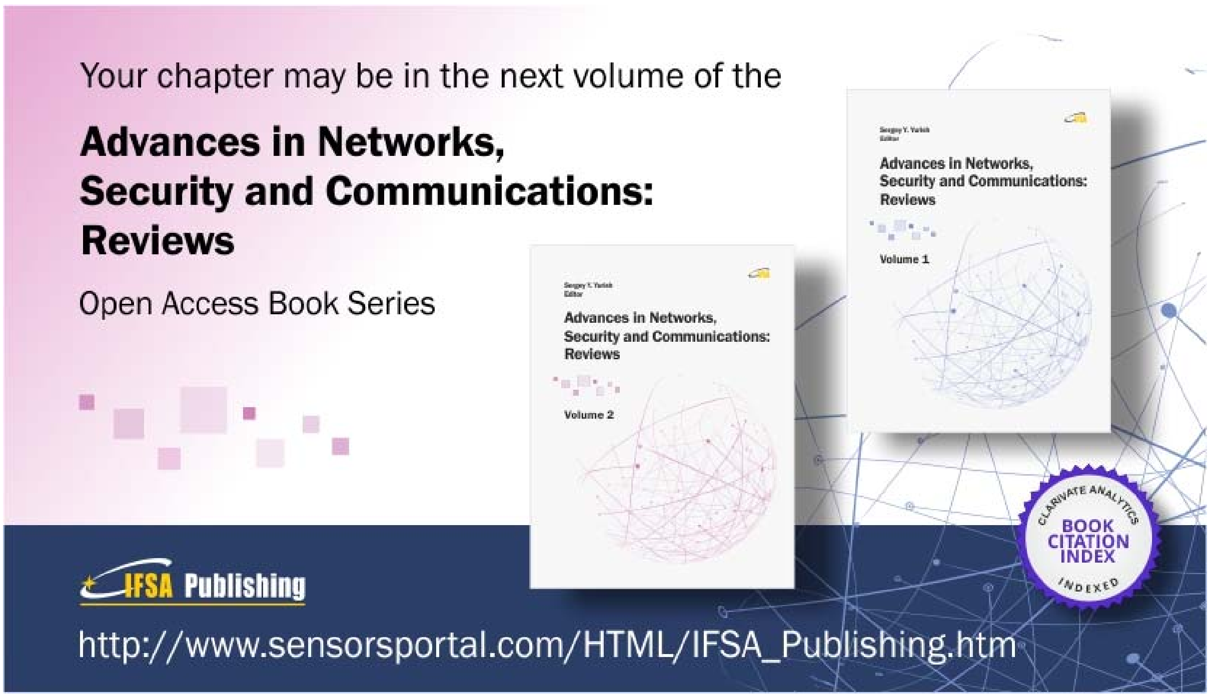

Sensors & Transducers, Vol. 266, Issue 3, August 2024, pp. 25-31

Sensors & Transducers

Published by IFSA Publishing, S. L., 2024
http://www.sensorsportal.com

Blue InGaN Lasers for Sensing and other Applications

[1, *] H. J. EICHLER, [2] S. STROHMAIER, [2] Th. RATAJ, [2] S. GRÜTZNER and [3] O. LUX

[1] Technische Universität Berlin, Institute of Optics and Atomic Physics,
Str. des 17.Juni 135, 10623 Berlin, Germany
[2] TRUMPF Laser SE, Volmerstr. 10, 12489 Berlin, Germany
[3] Deutsches Zentrum für Luft- und Raumfahrt, Institute of Atmospheric Physics,
Münchner Str. 20, 82234 Oberpfaffenhofen, Germany
Tel.: + 49 30 314 22498
[*] E-mail: joachim.eichler@tu-berlin.de

Received: 11 April 2024 / Reviewed: 7 June 2024 / Accepted: 27 June 2024 / Published: 31 August 2024

Abstract: InGaN diode lasers emit green, blue and violet wavelengths depending on the ratios of Indium, Gallium and Nitrogen atoms. Lasers with a lower fraction of Indium are commonly referred to as GaN lasers. Since around 1995, low-power GaN lasers have served as milliwatt light sources in Blu-ray players. Medium-power multimode lasers, capable of up to 50 Watts output, are employed for cutting and joining plastic and polymer materials. The short wavelengths of these lasers enable high-resolution imaging and sensing, making blue and violet lasers particularly valuable in microscopy and biomedical applications. In industrial contexts, high-power blue lasers emitting at 450 nm have become crucial for manufacturing batteries used in electric cars and airplanes. Currently, infrared solid-state and fiber lasers, pumped by infrared diodes, dominate applications such as drilling, cutting, welding and soldering. However, the significantly higher absorption of blue and green wavelengths by copper and other non-ferrous battery materials enhanced production efficiency. This has spurred the development of high-power blue lasers specifically for manufacturing tasks. The 450 nm wavelength of blue lasers results in more collimated beams compared to infrared counterparts, due to reduced diffraction. Combining laser beams from hundreds of single blue diodes by simple stacking allows the creation of laser systems with continuous output powers in the multiple kilowatt range. In pulsed operation, peak powers of up to 10 kW can be achieved. The compact nature of direct electrical excitation systems further enhances the appeal of blue lasers over fiber lasers in certain applications.

Keywords: GaN, InGaN, Laser diodes, Sensing applications, Broad area lasers, Stacking, High power laser systems.

1. Introduction

Blue-violet diode lasers based on GaN, with wavelengths around 405 nm, were initially developed for reading digital information from Blu-ray discs. In general, GaInP lasers cover a wavelength range from approximately 375 to 530 nm. Blue broad-stripe diodes emitting at 450 nm, with output powers up to 5 Watts, are utilized in projection systems and other applications. Higher powers are needed for material processing, which has led to stacking or spatial multiplexing of broad stripe laser emitters into modules capable of delivering more than 50 W. Laser bars are more compact and offer similar power levels as these modules. Multiplexing of modules or laser bars enables the construction of continuous-wave (cw) laser systems with outputs of 2 kW, with pulsed operation potentially achieving even higher powers.

Recently, high-power GaN lasers have found increasing use in material processing, particularly for the welding and soldering of copper. Despite the unique advantages of blue wavelengths over infrared (IR) in these applications, certain challenges remain to be addressed. This article provides an overview of the evolution of GaN lasers, tracing their commercial origins from 1-mW light sources in Blu-ray players to today's multi-kW systems. Notably, power efficiencies of up to 40 % and lifetimes exceeding 50,000 hours have been demonstrated [1].

In 2014, The Nobel Prize in Physics 2014 was awarded jointly to Isamu Akasaki, Hiroshi Amano and Shuji Nakamura "for the invention of efficient blue light-emitting diodes which has enabled bright and energy-saving white light sources". Their long-lasting research on GaN paved the way for the development of blue laser diodes at Nichia Ltd. in Japan.

2. Single Mode Laser with mW Power

A simplified sketch of an $In_xGa_{x-1}N$ laser emitting a cylindrical single transverse mode is shown in Fig. 1.

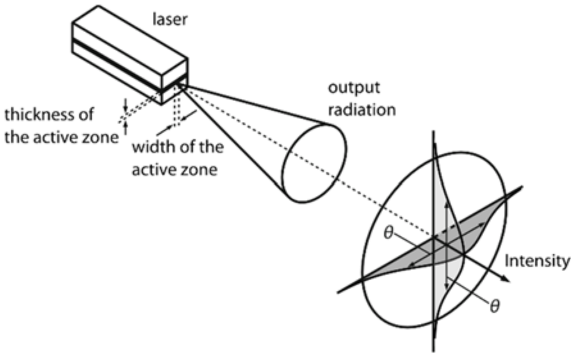

Fig. 1. A laser with a sufficiently small width of the active zone emits a beam with a circular, near-Gaussian intensity distribution with about equal divergence angles θ in the directions parallel and perpendicular to the active (gain) zone.

The chip structure of the laser diode typically consists of a substrate, such as InGaN, and several epitaxial layers including a light-generating quantum well layer of less than 10 nm thickness. Additional layers for wave guiding, current distribution, and metal contacts are also integrated. The chip design must enforce fundamental mode operation by ensuring lateral confinement of the laser beam, which is crucial for achieving the desired beam quality.

A very low threshold current is essential for these devices, as they often operate at high pulse frequencies and are thus usually biased near the threshold current. Achieving a low threshold current involves designing the mirrors with approximately 99 % reflectivity on the high-reflectivity (HR) side and about 90 % reflectivity on the output-coupling side.

GaN laser diodes were first widely applied in 1995 as light sources in Blu-ray players, emitting at 405 nm wavelength. This application requires low output power but demands single transversal mode operation (also referred to as fundamental, ground or basic mode) to ensure high beam quality [2, 3].

In the low output power range, single-mode lasers are also critical for near-to-eye projection systems used in augmented reality (AR) and virtual reality (VR) scenes where red, green and blue light sources are required [1].

The laser beam quality K of a cylindrical beam is reciprocal to the divergence angle θ and the beam waist radius w at the output facet. Therefore, the Beam Parameter Product BPP = w · θ is introduced. BPP is related to the beam propagation factor as follows:

$$M^2 = \pi \cdot BPP / \lambda = 1/K \qquad (1)$$

The best possible beam quality is K = 1 corresponding to a Gaussian intensity distribution of the fundamental transverse mode (TEM_{00} beam) with $M^2 = 1$.

3. Broad-area Single Emitter Laser Diodes

Blue diode laser chips are supplied by different companies such as Osram Corporation. Material parameters of GaN compared to GaAs are given in [1]. The GaN melting temperature amounts to 2500 °C and the surface hardness to 1200-1700 kg/mm². Melting point and hardness are twice as high as for GaAs. Fig. 2 illustrates the schematic design of our diode laser chips with the following characteristics:

- Laser chip dimensions: 3 to 4 × 0.5 mm;
- Type: Broad-area (or wide stripe) laser;
- Emitting stripe width: 20 µm (up to 50 µm);
- Front facet reflectivity: 1-5 %;
- Wavelength: 450 nm, range ±10 nm;
- Spectral linewidth: ~2 nm @ 3 W;
- Chirp: ~0,06 nm/K;
- Cooling water temperature: 20-30 °C;
- Threshold current: 300 mA;
- Maximum cw power: 5 W;
- Maximum cw efficiency: 40 %.

4. Laser Modules and Laser Bars

Single emitter diodes are stacked parallel (spatial multiplexing) to form so-called modules (consisting of 5 to 10 individual emitters) to increase the total output power. Diode chips are installed in module boxes, as shown in Fig. 3.

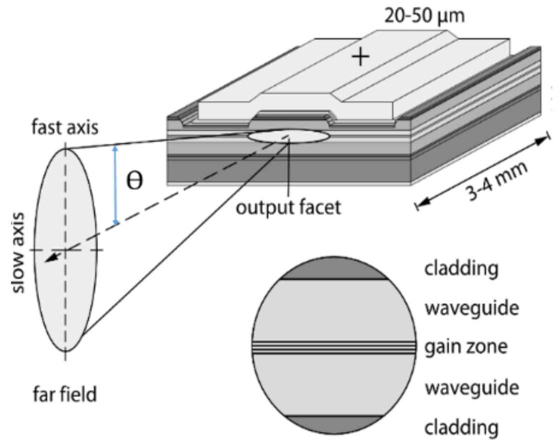

Fig. 2. General scheme of a broad-area diode laser with far field beam profile and sketch of the active waveguide structure. Due to the large width of the gain zone, the beam divergence angle θ in the slow axis direction is smaller than the fast axis divergence angle of an elliptical beam [1, 2].

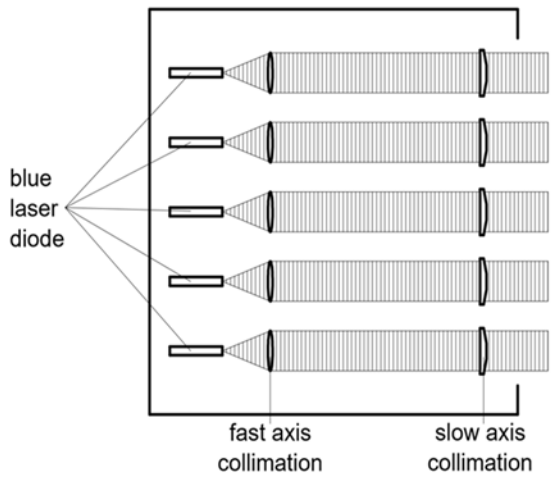

Fig. 3. Laser module consisting of five stacked single emitter diodes in a vacuum box. Cylindrical or aspherical lenses are used for collimation. Stacked laser beams pass a vacuum-tight window resulting in an increased power output of 50 W or more with a sufficient number of single emitter diodes.

Since the effective beam width of a laser module is large compared to the width of a single emitter diode, the beam parameter product BBP increases, and hence, the brightness (or brilliance) decreases.

High power output from a laser chip can also be achieved using laser bars, which typically consist of an array of single emitters. For example, a laser bar might include 23 emitters, each 400 µm wide, resulting in a total bar width of 9.2 mm and a cavity length of 1.2 mm on a single chip. A maximum output power of 107 W at 70 A was achieved from a single bar before thermal rollover. Additionally, a peak efficiency of 44 % was recorded at 90 W and 40 A [1]. Similar performance has been observed with broad-area single emitter lasers when stacked into modules.

5. Stacking Modules to kW Systems

The laser beams from multiple modules can be combined into a main beam using various multiplexing methods, as depicted in Fig. 4. We employed spatial multiplexing, similar to the approach used in stacked modules. This technique of stacking blue laser beams enables the creation of high-power laser systems. For example, blue cw laser systems have been developed with output powers of up to 2 kW.

In one setup, a laser beam transmitted through a 200 µm diameter fiber achieved a circular shape with an output power of 1.65 kW and a BPP of 20 mm·mrad. Operating the laser system at a lower power of 1.5 kW resulted in a BPP of 16 mm mrad, indicating improved beam quality (see Fig. 1). Higher powers up to 4 kW transmitted by a 600 µm fiber have been obtained by Laserline GmbH combining 10 bars.

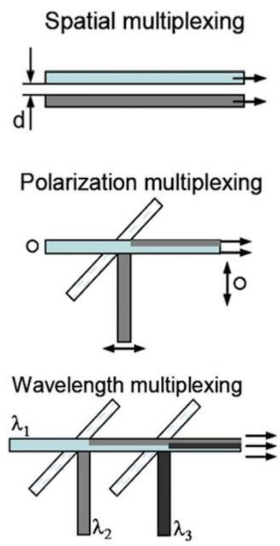

Fig. 4. Schematic multiplexing setups for laser beam combination [4].

Blue kW laser systems have been demonstrated by various providers, as summarized in Table 1. TRUMPF GmbH utilized broadband single emitters, which were stacked as shown in Fig. 3 to form modules. These modules were then further stacked or spatially multiplexed. The resulting beam was fed into a 200 µm diameter optical fiber, producing a circular output beam.

The output powers listed in Table 1 range from 1 to 4 kW. The highest power of 4 kW was achieved using a 600 µm transfer fiber. This large diameter results in the highest BPP of 30 mm·mrad and the lowest beam quality factor K ≈ 0.005 (see Eq. (1)). In contrast, the lowest output powers of about 1 kW were obtained with smaller BPP values leading to higher beam quality factors of approximately K ≈ 0.01. This relationship is expected, as K depends on the beam geometry.

Table 1. Key parameters of blue kW laser systems from different providers. The data of Laserline were given in a press report from May 31,2023. The data of Nuburu are given in an Internet report about the device Nuburu Bl-F™.

Provider	Max. cw power after fiber	Beam Parameter Product, fiber diameter	***Brightness*** $L = \pi^2 \cdot L$ W/(mm*mrad)
TRUMPF	1.15 kW	16 mm·mrad, 200 µm	4.5
TRUMPF	1.65 kW	20 mm·mrad, 200 µm	4.1
Laserline	4 kW	30 mm·mrad, 600 µm	4.4
Nuburu	1 kW	15 mm·mrad, 200 µm	4.4

Already in 2020, Nuburu reported a power of 1.5 kW with a BPP of 12 mm·mrad [5]. Additionally, Laserline GmbH in cooperation with Osram GmbH presented a 1000 W diode laser system emitting at 450 nm [6]. The beam from this system was coupled into and transmitted through a 1000 µm diameter optical fiber.

Besides the output power *P* also the brightness *L* of a laser beam is important for applications [2]. For a round or cylindrical laser beam behind the coupling fiber, *L* is defined as follows:

$$L = P/(\pi \cdot w \cdot \theta)^2 = L/\pi^2 \quad (2)$$

The average practiced brightness L of the lasers listed in Table 1 is L = (4.4 ± 0.2) $W/(mm \cdot mrad)^2$. We observed no significant difference in the performance of the kW laser system from TRUMPF, which was built using single broad-area laser emitters, compared to the results from Laserline and Nuburu, which utilized laser bars. Further investigations are necessary to enhance the power and brightness of the laser systems listed in Table 1.

For comparison, as early as 2019, Laserline reported powerful IR diode laser systems with wavelengths around 1 µm, offering standard outputs of up to 45 kW. The development of high-power laser systems in the IR range has primarily focused on dense wavelength multiplexing (DWM) systems, employing laser bars composed of multiple single emitters.

However, it is important to note that the failure rate of single blue lasers is higher than that of GaAs semiconductor lasers. Consequently, defective single lasers within a blue bar are anticipated. This issue can be mitigated by using selected and stacked single broad-area emitters instead of laser bars.

6. Power Limitation and Overpulsing

The output power of laser diodes is constrained by reversible rollover at high excitation currents [7], as well as by irreversible damage to the semiconductor waveguide and catastrophic optical mirror damage (COMD) [8, 9]. COMD occurs abruptly at a specific excitation current, leading to sudden failure. Thermal COMD suggests that significant power increases are possible in pulsed mode, where heating is generally much lower than in cw operation. However, non-thermal effects such as nonlinear absorption and other optical nonlinearities may also influence performance.

For a rough estimate, if the duty cycle is 10 %, the average temperature rise should be approximately 10 % of that in cw operation. This would imply that the peak current could be up to 10 times higher than the maximum permissible cw current, potentially leading to a tenfold increase in power. Thus, the maximum peak power during pulsed operation could be proportional to the inverse of the duty cycle. This rule is presumed to be valid only within certain limits of the laser output parameters.

High peak powers in pulsed operation can be achieved with multiple overpulsing at short pulse durations and low duty cycles. This has primarily been demonstrated with IR GaAs lasers [10-12]. For instance, the Ferdinand-Braun-Institute in Berlin has successfully overpulsed a single broad-stripe diode 8 times, achieving a peak power of 55 W with a 300 ns pulse duration.

Similar performance is anticipated for blue diode lasers. Consequently, it is expected that the multi-kW powers of continuous systems (Table 1) could be increased to over 10 kW in peak power during pulsed operation.

7. Applications of GaN Lasers

Blue GaN lasers, initially used in Blu-ray players, are now essential in fields such as medical diagnostics and treatment, illumination, projection, and environmental monitoring. Additionally, their advancement to high-power versions has made them vital for various material processing applications. The following sections will explore the diverse uses of GaN-based laser sources in detail.

Lasers for Blu-ray discs and data storage

The extensive commercial use of blue InGaN lasers began with their application as milliwatt light sources in Blu-ray players [13]. Blu-ray movies were first introduced in 2006, and by 2012, twelve million Blu-ray players were in consumer hands. However, with the rise of streaming services, the demand for Blu-ray discs and players appears to be saturating due to strong competition from digital downloads.

Blu-ray players utilize violet lasers at 405 nm wavelength, in contrast to the 780 nm wavelength used in CD players and the 650 nm wavelength used in DVD players. These players and recorders were also used as PC drives for permanent data storage but are increasingly being replaced by solid-state drives (SSDs). Further specifications of a typical Sony laser diode for Blu-ray applications are summarized in [13]:

- Diameter of housing: 3.8 mm;
- Laser output power: max. 200 mW (cw);
- Pulsed output power: max. 400 mW (30 ns, 50 % duty cycle allows twice the power);
- Beam divergence angles (slightly elliptical): $9^{\circ}/19^{\circ}$.

Medical sensing and laser treatment

Classical gas and solid-state lasers have been traditionally used for medical sensing applications, such as microscopy and flow cytometry [2]. However, these are increasingly being replaced by diode lasers, which enable the development of more compact diagnostic systems. InGaN lasers, in particular, are utilized for powerful fluorescence and Raman spectroscopy, aiding in cancer detection with the support of artificial intelligence (AI). Additionally, laser excitation spectroscopy is gaining traction in environmental quality monitoring [14].

In dermatology, laser treatment for skin diseases is performed using 5 W cw or pulsed dye lasers with wavelengths ranging from 400 to 800 nm. These lasers can be tuned to achieve penetration depths of up to several millimeters [2, p. 426]. Diode lasers offer the potential to construct even more convenient and versatile systems for medical treatments.

Illumination, projection systems, headlights

Currently, blue lasers in the single-digit watt range are employed for illumination applications by converting the 450 nm wavelength into various colors or white light for stage and show lighting. Automotive headlamps, which require power in the 10 W range, are commonly used in high-end vehicles.

For projection applications, such as those in business environments or cinemas, power levels of approximately 100 W per package are becoming increasingly relevant [15]. Additionally, low-power single-mode lasers are used for near-to-eye AR and VR projection, enhancing the visual experience for virtual and artificial reality scenes.

Material processing

Blue lasers with high power and brightness are increasingly important for manufacturing applications, particularly for processing materials such as copper, aluminum, and gold, which are used in the construction of batteries for electric vehicles and possibly airplanes [5, 16]. Thin copper foils and thick connectors are commonly processed for various consumer electronic devices. Currently, near-IR solid-state and fiber lasers pumped by IR diodes are used for drilling, cutting, welding and soldering. However, blue and green lasers offer significant advantages due to their higher absorption in non-ferrous materials. For instance, the absorption of blue light (around 450 nm) by copper and other non-ferrous battery materials can be over 10 times greater than that of IR light at approximately 1 μm wavelength. This enhanced absorption allows for greater production efficiencies, making high-power blue lasers increasingly relevant for manufacturing. The short wavelength of 450 nm additionally results in more collimated beams due to reduced diffraction compared to IR lasers.

Currently, blue broad-stripe diodes at 450 nm and output powers up to 5 W are available for projection systems and other applications. For material processing, higher power levels are obtained with broad-stripe laser emitters that are either stacked or spatially multiplexed into modules, achieving output powers above 50 W. More compact laser bars can deliver similar power levels. By multiplexing or combining beams from these modules or laser bars, cw laser systems with outputs of up to 4 kW can be constructed (see Table 1). Pulsed operation could potentially achieve peak powers of up to 10 kW.

Power levels of 1 kW and above are necessary for effective cutting, welding, and soldering [1]. The development of IR lasers and laser systems took several decades, with advancements in semiconductor chips, packaging technology, materials, and optics all contributing to the development of multi-kW systems. In contrast, the development of GaN-based blue lasers for power applications began after 2000 and has progressed more rapidly. Many of the building blocks developed for IR systems were applicable to 450 nm blue laser systems.

While IR lasers started with short resonator lengths of 300 μm, narrow emitters, and smaller die, they have evolved to resonator lengths of 4 to 6 mm and fill factors of 70 % or more in 10 mm wide laser bars [1]. Today's GaN lasers are still in the early stages of development compared to these features. GaN-based blue lasers for 450 nm light currently exhibit lower efficiency and total output power compared to GaAs-based IR systems. Additionally, production costs remain higher, and production yield for AlGaN devices is lower. However, GaN lasers offer the unique advantage of effective absorption of blue or UV light in materials that poorly absorb IR light [1]. Specific examples of material processing with blue lasers are detailed in references [17-20].

Pulsed high peak powers are expected to further enhance process efficiencies. By using pulsed lasers, the same processing results can often be achieved with less energy input. Pulses allow for more precise material processing, as they result in lower heating and reduce the disruptive absorption of laser light by vaporized metallic plasma. These are significant advantages over the continuous processing systems currently available on the market. Consequently, pulsed blue diode lasers are anticipated to complement cw lasers in specialized applications.

Optical excitation of solid-state lasers

Blue and green InGaN lasers are valuable for pumping Titanium sapphire (TiSa), Pr^{3+} , and other solid-state lasers, offering a simpler alternative to more complex frequency-doubled Neodymium pump lasers [21]. TiSa lasers, which emit ultrashort pulses with Petawatt peak power, are currently of great interest in basic research. InGaN semiconductor lasers, with their capability for direct electrical pumping, are expected to significantly enhance the overall efficiency of various solid-state lasers.

Sensing

GaN diode lasers emitting in the blue spectral range are commercially available and provide sufficient optical output for spectroscopic applications but suffer from non-wavelength-stabilized broadband spectral emission. To address this limitation, efforts have focused on developing tunable sources using external cavity devices with mechanically adjustable gratings. These advancements have achieved output powers of up to 500 mW with high wavelength stability, making the lasers particularly suitable for applications requiring high precision and sensitivity [22, 23].

Blue diode lasers, sometimes realized as vertical cavity surface emitting lasers (VCSELs), are utilized as biosensors based on Raman spectroscopy, where their specific wavelengths enable the detection and quantification of trace gases in the atmosphere. This capability is crucial for monitoring air quality, identifying pollutants, and ensuring environmental compliance. In the biomedical field, GaN lasers are used in fluorescence spectroscopy and imaging to excite fluorescence in biological samples, which is essential for detecting and analyzing biomolecules, cells, and tissues, aiding in early disease diagnosis.

Water quality monitoring systems also benefit from blue lasers due to their ability to detect contaminants through fluorescence-based sensing techniques. These lasers provide rapid and accurate assessments of water purity, ensuring safe drinking water and environmental health. Similarly, blue GaN lasers are employed to detect harmful substances in food products through fluorescence sensing, playing a critical role in preventing foodborne illnesses and safeguarding public health.

The industrial sector utilizes blue GaN lasers for monitoring processes with high precision, including the measurement of chemical compositions and gas concentrations. This precision is essential for optimizing manufacturing processes, enhancing product quality, and maintaining safety standards.

Blue GaN lasers are also of interest for lidar (light detection and ranging) systems in various remote sensing applications. Their specific wavelengths enable accurate distance measurements and detailed environmental mapping, particularly underwater due to low absorption. Additionally, GaN lasers are used in smart headlights in combination with modules for autonomous vehicle navigation based on lidar [24].

9. Summary and Conclusions

Blue lasers are advantageous for efficiently processing non-ferrous metals such as copper, aluminum, and gold. High efficiencies and rapid process speeds can be achieved with blue lasers in cutting, welding, soldering, and surface structuring of battery materials, necessitating laser systems that emit power in the kilowatt range. Such systems have been developed by TRUMPF GmbH by combining the beams from a large number of single broad-area diode lasers.

To construct these high-power systems, approximately 10 parallel individual emitters are mounted on a base plate within a vacuum-tight housing. The laser module also integrates collimating lenses. The beams from about 50 such modules are then combined to form the final output beam. This approach has enabled the creation of blue cw laser systems with output powers up to 2 kW. A laser beam transmitted through a 200 µm diameter fiber achieved a circular shape with an output power of up to 1.65 kW and a brightness of 4.1 to 4.5 W/(mm mrad)².

Further advancements have been demonstrated by Laserline GmbH in cooperation with Osram GmbH, achieving up to 4 kW of laser power with a brightness of 4.4 W/(mm mrad)² using a 600 µm diameter fiber. This system utilized laser bars instead of the stacked single emitter modules employed by TRUMPF.

Ongoing progress in blue diode laser technology, building on the pioneering research of Nakamura and colleagues, is expected to continue advancing the field [25]. Applications of blue diode lasers, ranging from low to high power, are broadening, particularly in industrial processing.

References

[1]. M. Beringer, H. König, Blue high-power laser diodes-beam sources for novel applications, *PhotonicsViews*, Vol. 2, Issue 2, 2020, pp. 60-63.

[2]. H. J. Eichler, J. Eichler, O. Lux, Lasers – Basics, Advances and Applications, *Springer*, 2018.

[3]. Y. Hu, S. Liu, C. Hu, Y. Xiao, P. Zhou, H. Peng, X. Tang, Mode analysis and measurement of single-emitter blue diode lasers, *Appl. Opt.*, Vol. 62, Issue 23, 2023, pp. 6264-6274.

[4]. H. Schlüter, C. Tillkorn, U. Bonna, G. Charache, J. Hostetler, T. Li, C. Miester, R. Roff, T. Vethake, C. Schnitzler, Dense spatial multiplexing enables high brightness multi-kW diode laser systems, *Proceedings of SPIE*, Vol. 6104, 2006, 61040M.

[5]. J.-M. Pelaprat, M. Zediker, M. Finuf, R. Fritz, The blue light district, *PhotonicsViews*, Vol. 17, Issue 1, 2020, pp. 61-65.

[6]. M. Baumann, A. Balck, J. Malchus, R. V. Chacko, S. Marfels, U. Witte, D. Dinakaran, S. Ocylok, M. Weinbach, C. Bachert, A. Kösters, V. Krause, H. König, A. Lell, B. Stojetz, M. Ali, U. Strauss, 1000 W blue fiber coupled diode-laser emitting at 450 nm, *Proceedings of SPIE*, Vol. 10900, 2019, 1090005.

[7]. H. König, A. Lell, B. Stojetz, M. Ali , C. Eichler, M. Peter, A. Löffler, U. Strauss, M. Baumann, A. Balck, J. Malchus, V. Krause, Blue 450 nm high power semiconductor continuous wave laser bars exceeding rollover output power of 80 W, *Proceedings of SPIE*, Vol. 10514, 2018, 1051402.

[8]. L. Díaz, H. J. Eichler, K. Weich, A. Klehr, U. Zeimer, Internal defect localization in 980 nm ridge waveguide lasers, *Proceedings of SPIE*, Vol. 6193, 2006, 61930G.

[9]. Using Visible InGaN Laser Diodes, Application Note Document, AN101, *AMS-OSRAM AG*, 2022-10-17.

[10]. P. Crump, G. Tränkle, A brief history of kilowatt-class diode-laser bars, *Proceedings of SPIE*, Vol. 11301, 2020, 113011D.

[11]. A. Boni, H. Wenzel, P. Crump, Capture time as a limit to pulsed power in 940 nm broad area diode lasers, in *Proceedings of the IEEE Photonics Conference (IPC'22)*, 2022, Canada, pp. 1-2.

[12]. A. Pietrzak, P. Crump, H. Wenzel, R. Staske, G. Erbert, G. Traenkle, 55 W peak power from 1100 nm wavelength 60 µm broad-area laser diodes enabled by reduced carrier accumulation in the waveguide, *Semicond. Sci. Technol.*, Vol. 24, 2009, 035020.

[13]. Blu-ray, https://en.wikipedia.org/wiki/Blu-ray

[14]. D.-E. Zacharioudaki, I. Fitilis, M. Kotti, Review of Fluorescence Spectroscopy in Environmental Quality Applications, *Molecules*, Vol. 27, Issue 15, 2022, 4801.

[15]. A. Loeffler, C. Eichler, J. Mueller, S. Gerhard, B. Stojetz, S. Tautz, C. Vierheilig, J. Ristic, A. Avramescu, M. Horn, T. Hager, C. Walter, T. Dobbertin, H. Koenig, U. Strauss, InGaN power laser chips in a novel 50 W multi-die package, *Proceedings of SPIE*, Vol. 9363, 2015, 936318.

[16]. H. J. Eichler, S. Strohmaier, Blue kW laser systems by spatial multiplexing single InGaN diodes, in *Proceedings of the 7th International Conference on Optics, Photonics and Lasers (OPAL'24)*, Palma de Mallorca, Spain, 15-17 May, 2024, pp. 132-134.

[17]. T. Ryba, T. Stempky, Advances in green laser processing, Industrial Laser Solutions, https://www.laserfocusworld.com/industrial-laser-solutions/article/14221988/advances-in-green-laser-processing

[18]. M. Finuf, W. C. Gray, M. S. Zediker, R. D. Fritz, Methods and Systems for Welding Copper Using Blue Laser, Patent US10940562B2, *USA*, 2021.

[19]. O. Bocksrocker, T. Hesse, Method for Joining Copper Hairpins and Stator, Patent WO2020165142A1, *WIPO (PCT)*, 2020.

[20]. S, Strohmaier, T. Rataj, A. Popp, B. Schmidt, Laser Soldering for Connecting Electronic Components, Patent DE102020201950A1, *Germany*, 2021

[21]. P. Wang, Q. Yuan, R. Xia, S. Xu, Y. Xiao, X. Tang, Thermal effect analysis on cuboid Pr:YLF crystals pumped by blue laser diodes, *Appl. Opt.*, Vol. 62, Issue 18, 2023, pp. 4797-4804.

[22]. N. Ruhnke, A. Müller, B. Eppich, M. Maiwald, B. Sumpf, G. Erbert, G. Tränkle, 400 mW external cavity diode laser with narrowband emission at 445 nm, *Opt. Lett.*, Vol. 39, Issue 13, 2014, pp. 3794-3797.

[23]. B. Li, S. Luo, A. Yu, J. Gao, P. Sun, X. Wang, D. Zuo, Sensitive Raman gas analysis using a 500 mW external cavity diode laser at 410 nm, *Laser Phys. Lett.*, Vol. 14, Issue 9, 2017, 95701.

[24]. S. Donati, W.-H. Cheng, C.-N. Liu, H.-K. Shih, Z. Pei, Embedding LiDAR and smart laser headlight in a compact module for autonomous driving, *OSA Continuum*, Vol. 4, Issue 5, 2021, pp. 1587-1597.

[25]. S. Nakamura, S. Pearton, G. Fasol, The Blue Laser Diode – GaN Based Light Emitters and Lasers, *Springer*, 1997.